DeepLandforms: A Deep Learning Computer Vision toolset applied to a prime use case for mapping planetary skylights

Giacomo Nodjoumi[1*], Riccardo Pozzobon[2,3], Francesco Sauro[4], Angelo Pio Rossi[1]

[1]Jacobs University Bremen gGmbH, Bremen, Germany

[2]INAF-Astronomical Observatory of Padova, Padova, Italy

[3]Department of Geosciences, University of Padova, Padova, Italy

[4]Department of Biological, Geological and Environmental Sciences, University of Bologna, Bologna, Italy

Corresponding author: Giacomo Nodjoumi (g.nodjoumi@jacobs-university.de)

Key Points:

- Instance Segmentation methodology is used to map landforms obtaining vectorial data in geopackage file format.
- A newly developed composite toolset to perform the image pre-processing, data labeling, model training and inference tasks, is presented.
- The results of a prime case of mapping pit and skylights on Mars surface are showed.

Abstract

Thematic map creation is a process that implies several steps to be accomplished regardless of the type of the map to be produced, starting from data collection, through data exploitation and ending with maps publication as print, image, and GIS format. An example are geological, lithological, and geomorphological maps, in which most of the highest time-consuming tasks are those related to the discretization of single objects by identifying a set of unique characteristics that describe uniquely those objects. Commonly these tasks introduce interpretative biases due to the different experience of the mappers who's performing it. In this setting, Deep Learning Computer Vision techniques could play a key-role but lack the availability of a complete set of tools specific for planetary mapping. The aim of this work is to develop a comprehensive set of ready-to-use tools for landforms mapping, in which users have full access to the workflow and over all the processes involved, granting complete control and customization capabilities. In this work are presented both the developed tools and the approach that has been used and that is based on consolidated Deep Learning methodologies and open-source libraries commonly applied in other fields of Computer Vision. The toolset and the approach presented have been tested in the science case of mapping sinkhole-like landforms on Mars and results are presented.

Plain Language Summary

The creation of maps is a complex set of several tasks that, regardless of the type of the map, are often very time-consuming. For instance, all the occurrences of a specific object, natural or man-made in a defined area, needs to be identified, drawn and classified manually; a work that can be easily accomplished for large object in small areas but may be unmanageable in cases such the mapping of small landforms on the entire surface of a planet or moon. Nowadays, especially on Earth, several of the above tasks takes adavantages of highly specialized computer codes based on Deep Learning systems. Such codes are almost never ready-to-use, and require higher knowledge in computer programming languages. In this work we present the first release of a novel open-source computer software, almost ready-to-use, that provides all the instruments for creating or directly using custom Deep Learning models for automatic landforms mapping. We present also the results obtained by trying this software using data of Mars's surface with the aim of mapping sinkhole-like landforms.

1. Introduction

The exploration of terrestrial planets in the Solar System was and still is performed mainly on data that cover almost all the electromagnetic spectrum, acquired over the last century by several types of orbiters, rovers, and landers. Planetary data volumes are constantly increasing both in quality and quantity, with the contribution of both public and private entities.

Imagery has always been the primary resource for researchers in planetary sciences, especially for geologists and geomorphologists. In the last two decades the progress in the development of very high-resolution image sensors gave access to the community to images with a spatial resolution in the order of centimeters. Data collected by High Resolution Imaging Science Experiment (HiRISE) instrument, on board of the Mars Reconnaissance Orbiter (MRO) (McEwen et al., 2007) or by the Narrow Angle Camera (NAC) experiment, on board of Lunar Reconnaissance Orbiter (LRO) (Robinson et al., 2010), have been used in several works related on their planetary body.

These include not only publications related to specific surface's features such as the impact of megabreccia (Grant et al., 2008), crater counting and morphometry (Benedix et al., 2020; Chen et al., 2017; Robbins & Hynek, 2014; Servis et al., 2020; Watters et al., 2015), boulder counting (Le Mouélic et al., 2020; Sargeant et al., 2020; Watkins et al., 2017) characterization of polar layered deposits (Milkovich et al., 2009), identification of the source of ice blocks in the north polar cap (Su et al., 2021) but also comparative analyses and numerical modeling (Guimpier et al., 2021), analyses of Mars's surface processes (Guallini et al., 2018; Luzzi et al., 2020) including skylight, pits (Barlow et al., 2017; Cushing et al., 2015; Michikami et al., 2014; Xiao et al., 2014), pit chains (Wyrick, 2004) , and more advanced application such as Structure-from-Motion (SfM), (Le Mouélic et al., 2020; Micheletti et al., 2015; Muller et al., 2021; Y. Wang et al., 2021), Shapes-from-Shading (SfS) (Alexandrov & Beyer, 2018; Lohse et al., 2006), Machine Learning for object detection and classification (Barrett et al., 2022; Dundar et al., 2019; Hipperson et al., 2020, 2020; Hu et al., 2021; Lee, 2019; Nodjoumi et al., 2021; Palafox et al., 2017; Rashno et al., 2017; Silburt et al., 2019; Wilhelm et al., 2020).

This leap in image quality and quantity has introduced new challenges for researcher since the higher resolutions brought the great advantage of being able to analyze the surface of those planets with unprecedented details, retrieving useful information of various field such the characterization of Martian and lunar pits (Cushing et al., 2015; Haruyama et al., 2009; Kaku et al., 2017; Sharma & Srivastava, 2021; Wyrick, 2004; Xiao et al., 2014) or the Recurring Slope Linae (RSL) (McEwen et al., 2021), but with several downsides, for instance, larger image size ad numbers of acquisitions available may create problems for large scale processing due to the computational power requirements.

Map production is a complex set of tasks performed by teams and groups of researchers specialized in single to multiple fields that combine their knowledge in order to describe and characterize the surface of a planet ('Geomorphological Mapping', 2013; Napieralski et al., 2013; Nass et al., 2021). Depending on the type of the map in production, these tasks may vary a lot but at least four major focal tasks are shared across all map types: a) data collection, b) data exploitation , c) map creation, d) map dissemination (Naß et al., 2017, 2021). Among those major tasks, the most time-consuming sub-tasks are the definition of the standards for the map production and dissemination (Hare et al., 2018) and the proper digital creation of the map elements by manual drawing all the features of the area of interest using GIS software. For instance, in geomorphological mapping, the main target is the identification of landforms. With the term landform, is intended a topographic expression of the surface of a planetary body that can be described by at least seven parameters, shape, size, height, texture, pattern, tone/hue, location/association (Tempfli et al., 2009) that combined generate a unique object while Multiple landforms in an area describe a terrain (Bridge & Demicco, 2008; DiPietro, 2013). See Table S1 in supporting information.

Genetic mechanisms are a complex combination of interconnected processes and forces, some of which are more wide and planetary-scale dependent. For instance gravity usually drives the size of different morphologies such as lava tubes and rilles on the Moon, Mars and Earth (Bardabelias et al., 2020; Chappaz et al., 2017; Cruikshank & Wood, 1972; Greeley, 1971; Haruyama et al., 2009; Horvath et al., 2020; Kaku et al., 2017; Léveillé & Datta, 2010; F. Sauro et al., 2020; Whitten & Martin, 2019). Other mechanisms are more related to the presence of specific environmental and atmospheric characteristics and may drive different subtypes of a common landform type.

Among the many examples, landforms such as landslides (Hungr et al., 2014) and sinkholes (Parise, 2019) found on Mars (Bardabelias et al., 2020; Cushing et al., 2007; De Blasio, 2011; Guimpier et al., 2021; Hooper & Smart, 2013; Sharma & Srivastava, 2021), may have some formation and driving mechanisms in common to their respective landforms found on Earth (Acharya et al., 2006; Díaz Michelena et al., 2020; Gutiérrez et al., 2008; Hungr et al., 2014; Jiang, 2020; Parise, 2019; U. Sauro, 2016; Van Den Eeckhaut et al., 2007; Youssef et al., 2012). Those mechanisms and settings may be related to similar surface and subsurface characteristics and properties such as the geological settings, type of substratum, the average slope, and the solar exposure of the area.

Conversely, the presence of liquid-water seasonal precipitation and groundwater circulation, on landslides and sinkholes found on Earth is not only a driving mechanism but may also act as a trigger for the process (Allemand et al., 2011; Alonso et al., 2010; Cahalan & Milewski, 2018; Díaz Michelena et al., 2020; Duhart et al., 2019; Gutiérrez et al., 2008; Jiang, 2020; Lacerda et al., 2004; Lin et al., 2004; Van Den Eeckhaut et al., 2007; Youssef et al., 2012), while it is still under debate on those found on Mars (De Blasio, 2011; Guimpier et al., 2021; Hooper & Smart, 2013; Salese et al., 2019; Smith et al., 2006).

Several types of terrains and thus landforms exist, natural and artificial, some are peculiar to specific areas or even planets or moons, others can be found in almost all planetary bodies of the Solar System (Hargitai & Kereszturi, 2015a).

In general terms, the occurrence of specific landforms are deeply connected to the geology of the area, the past and present atmospheric processes and, at least on Earth, by anthropological activities (this applies to a certain extent also to robotic or human landing sites) (Brierley et al., 2021; James et al., 2013; Slaymaker et al., 2021). Studying those features is essential to better know the relations between those three main major processes and characteristics and the evolution of the area.

Identification, classification and description of landforms is done by mappers using multiple data types and sources such as images in various spectra, previous maps, digital elevation models and so on (Luzzi et al., 2020; Parente et al., 2019; Sivakumar et al., 2017). The time necessary to accomplish this specific sub-task is strictly dependent on the scale of the area of interest and scale of the features in it since wider areas and smaller features may lead to extremely high workloads. The final map product is a fundamental element to consider while estimating the complexity of the map production work. This is due to the wide diversity of map products available, and thus to the parameters to be defined and the data to be collected and processed

Indeed, geological maps takes into account spatial-temporal relations between surface and subsurface's features, their compositions and the past and present geological processes involved (Martinot et al., 2018; Naß & van Gasselt, 2021; Pondrelli et al., 2020; Sun & Stack, 2020; Tsibulskaya et al., 2020), while geomorphological maps takes the same parameters at a higher level, more related to the visual properties derived by the acquired images like colors, texture, patterns and so on (Kumar et al., 2019; Tirsch et al., 2021; Tsibulskaya et al., 2020; B. Wu et al., 2020).

In addition, regardless of the type of map, the data collection steps can be very time-consuming tasks, beyond being also complex, since most of the available data needs to be pre-processed prior to the proper analysis. For example, there are more than 1.8 million products of HiRISE acquisitions that are roughly more than 49 Terabyte for a single imager that is still acquiring data at the time of writing.

In this framework, Deep Learning computer vision methodologies, are robust and widely accepted and applied both on Earth for crops monitoring and management (Grace et al., 2021), land use (Rousset et al., 2021; Talukdar et al., 2020), risk management and assessment (Ghorbanzadeh et al., 2019; Liu et al., 2004; Merghadi et al., 2020; Paul & Ganju, 2021; Tien Bui et al., 2016; Yousefi et al., 2020); and on other Solar System planetary body (Barrett et al., 2022; Dundar et al., 2019; Hipperson et al., 2020, 2020; Lee, 2019; Palafox et al., 2017; Rashno et al., 2017; Stepinski et al., 2007; S. Wang et al., 2020; Wilhelm et al., 2020); thus may be play a crucial role in exploiting such amount of data.

The objectives of these methodologies are mainly of four types listed below and shown in Figure 1.

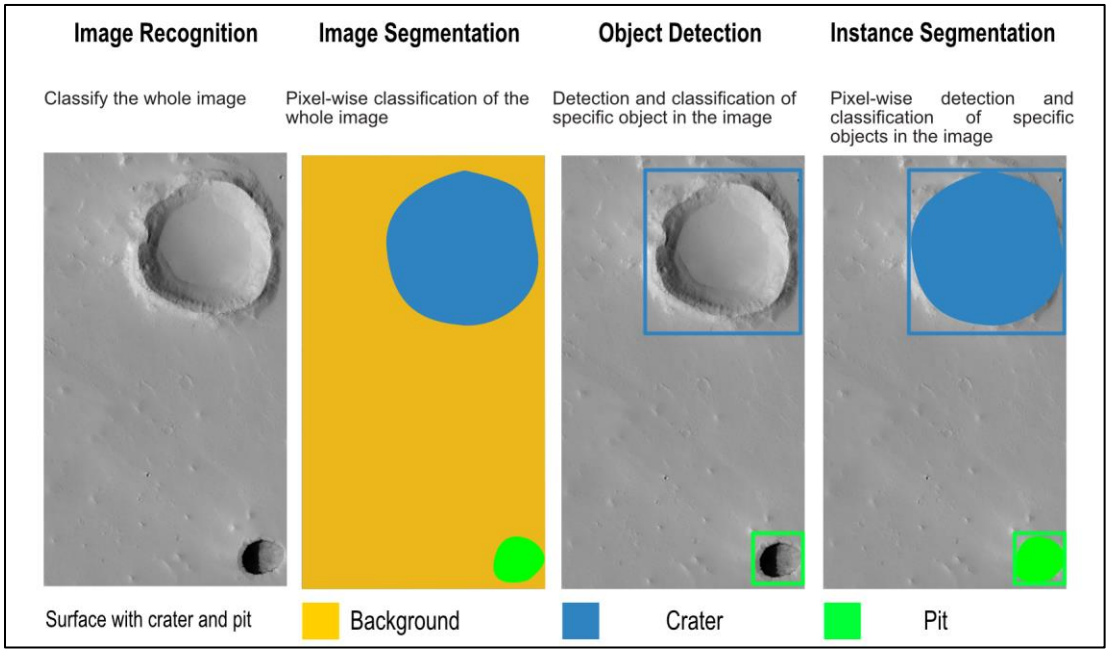

Figure 1. Comparison between image recognition, image segmentation, object detection and instance segmentation for the specific case of geomorphology mapping.

The first methodology displayed in Figure 1 is the I*mage Recognition (ImR)* which classifies the whole image contents, the second, called I*mage Segmentation (ImS)*, classifies each pixel of the image and create segments of adiacent pixels with contiguous classification. The third technique, the O*bject Detection (OD)*, locate the objects using bounding boxes and classifies them separately, while the fourth, the I*nstance Segmentation (InS)* is a combination of the second and the third method, obtaining the segmentation of only the objects identified by the detection.

Those architectures may require a tremendous amount of well labeled training data in order to generalize properly the model and avoid overfitting and underfitting problems (Zhang et al., 2021). More detailed descriptions are available in the supporting information Text S1.

Such data, are not always ready-to-use for labeling, mostly due to compatibility issues between labeling software, deep learning software and data itself. More specifically, these issues are related mainly to data size and format, and therefore pre-processing tasks have a key role and are mandatory for any approach especially if georeferencing

information is required. A more detailed overview is provided in the supporting information Text S3 along with detailed pre-processing steps.

Nowadays, Deep Learning methodologies are widely and commonly used as a solution to solve several daily problems, for instance facial recognition features of social networks, Google images search, security surveillance and much more, but also specific problems relative to Earth Observation such as land coverage, crops vegetation monitoring, early warning systems and other (Brust et al., 2019; Hoeser & Kuenzer, 2020; Miyamoto et al., 2018; Redmon et al., 2016; Szegedy et al., 2013; Y. Wu et al., 2019a, 2020; Zhao et al., 2019).

In the last two decades a lot of efforts have been made to use Deep Learning to solve planetary mapping problems on Earth (Liu et al., 2004; Paul & Ganju, 2021; Stepinski et al., 2007; Talukdar et al., 2020) as like as on Mars (Hipperson et al., 2020; Nagle-McNaughton et al., 2020; Palafox et al., 2017; Wilhelm et al., 2020) and the Moon (Hu et al., 2021; Silburt et al., 2019; S. Wang et al., 2020) exploring almost all architectures and algorithms with very promising results. In some cases the code used for the analysis is publicly available (Aye et al., 2019; Barrett et al., 2022; Lee, 2019; Silburt, 2017/2019; Wilhelm et al., 2020) and may be used to create preliminary map products.

The results obtained with the above-mentioned codes are typically plain images with superimposed the bounding boxes or the segmented area and are in non-georeferenced raster file type formats such as png or jpeg. Those type of results need to be georeferenced before being further processed in GIS software to vectorize manually all the objects or segments and finally obtain a vectorial map that can be published in a geospatial data format such as OGC Geopackage. This newer file format is specific for transferring geospatial information similarly to ESRI shapefiles (ESRI technical document, 1998), but with higher portability and compactness, moreover is an open format and standard-based (Open Geospatial Consortium, 2021).

For instance, segmented areas such those that represent geomorphological units, need to be manually digitized as individual shapes in GIS software, with the manual conversion and assignment of the properties of the units in the image.

In this setting, geologists and geomorphologists, not familiar with programming languages and interested only in workflows and tools may have a lot of difficulties understanding and using complex machine learning approaches that require higher knowledge in computer science, especially if complete and ready-to-use tools are not available.

In this work is presented a first complete working release of *DeepLandforms*, a set of comprehensive and ready-to-use tools specifically developed for planetary mapping.

This toolset is a follow-up of the work and tool (Nodjoumi et al., 2021) based on object detection methodology and focused on the usage of You Only Look Once version 5 (YOLOv5) framework (Pham et al., 2020; *Ultralytics/Yolov5*, 2020/2021) to detect sinkhole-like landforms on Mars, obtaining a geopackage containing, the centroid coordinates of the bounding boxes, confidence level and classification class for each of the detections. In Figure 2 the map showing both the MGC^3 catalog and the object detection results.

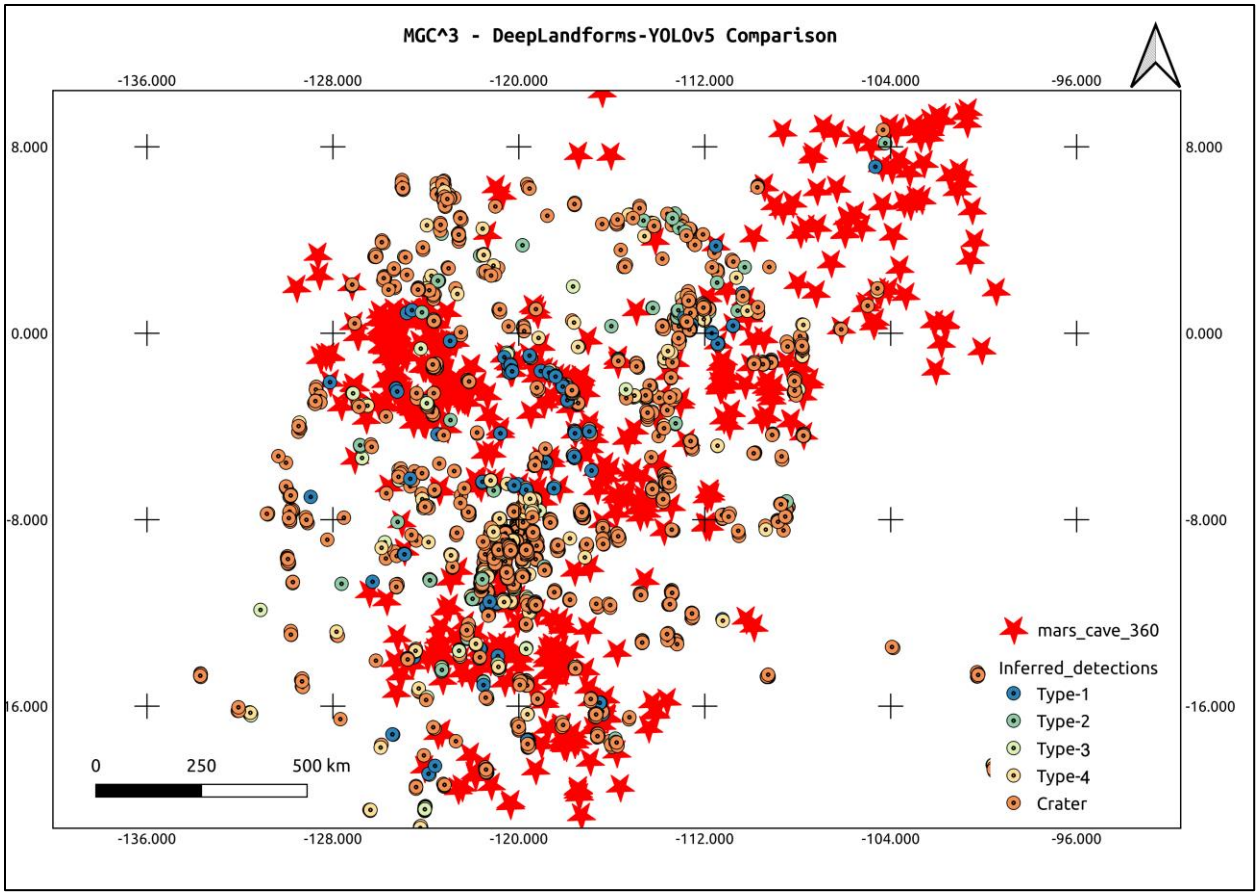

Figure 2. Comparison of MGC^3 catalog and results obtained by using Deep Learning object detection (DeepLandforms-YOLOv5) on a similar dataset (Nodjoumi et al., 2021).

Despite centroid coordinates could be considered a starting point for proper mapping, there is the lack of the spatial dimensionality thus providing only a general localization of the features, even using the coordinates of the detection boxes there is still the lack of a precise localization and definition of the shapes of the landforms. To further improve the previous work, a change of architecture was mandatory, moving from object detection to instance segmentation architecture.

The instance segmentation library selected for this work is the Detectron2 Library, developed and periodically maintained by the Facebook AI Research team, specialized in image segmentation tasks through R-CNN networks. See supporting information Text S2 for additional details on Detectron2 Library.

In this work, the Mask R-CNN network has been considered the only main network since it is specific for object instance segmentation tasks (He et al., 2018).

Mask R-CNN extends Faster R-CNN, class labels and bounding boxes, by adding a third output, the objects masks (He et al., 2018; Massa & Girshick, 2018). A mask can be considered as a method of describing an image in boolean-based representation by using specific filters or functions, meaning that the content of the image will be converted in

only two possible values (0-1, on-off, true-false, and so on). See supporting information Text S5 and Figure S1. Each mask is then characterized by internal and external values and can be localized by using image pixel coordinates.

2. DeepLandforms

DeepLandforms has been developed with the aim of creating a comprehensive set of tools to support a complete workflow for mapping landforms using georeferenced data and producing results in vectorial format. Flowchart of the workflow can be visualized in Figure 3.

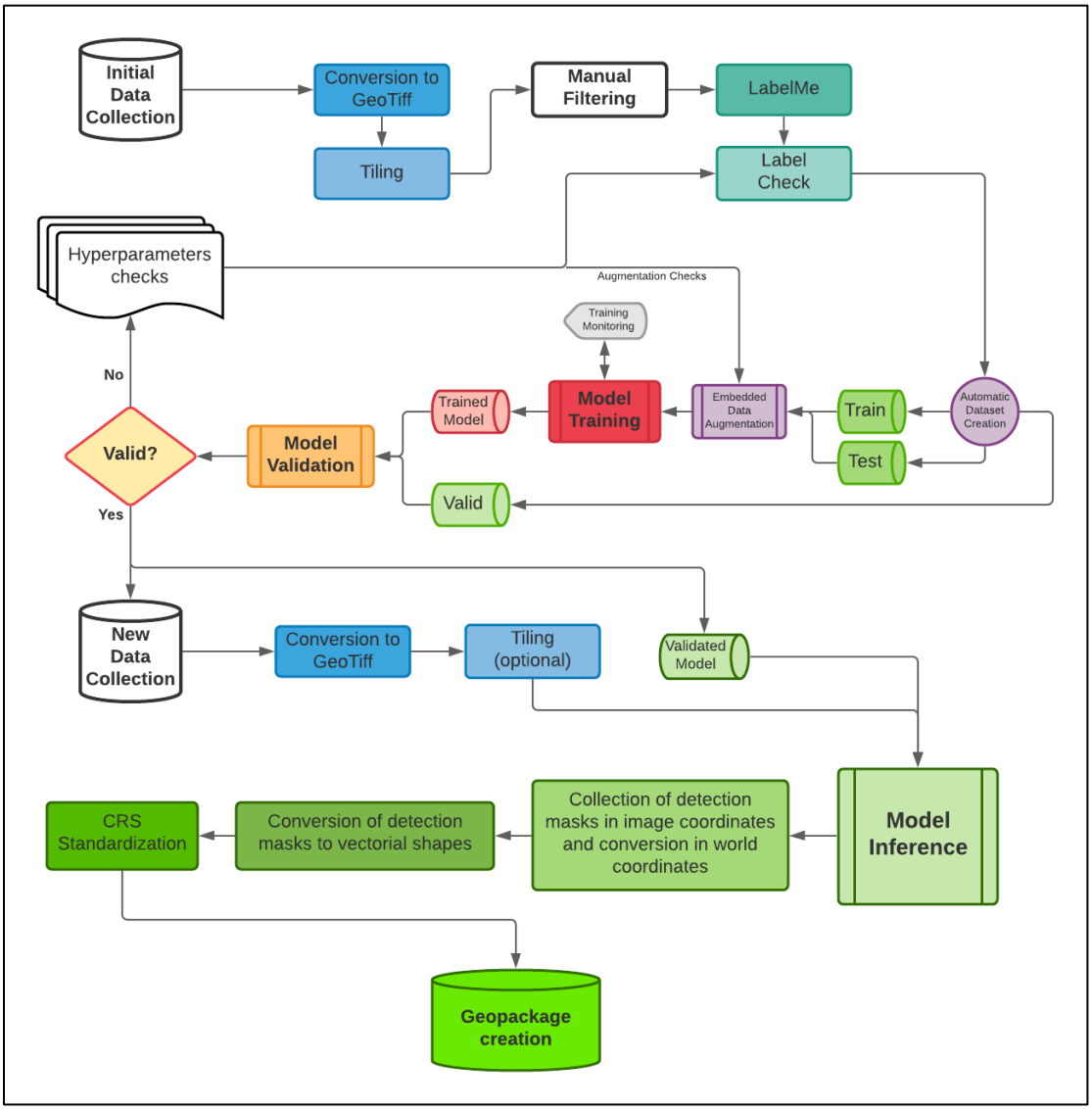

Figure 3. Flowchart of the complete workflow on which is based the DeepLandforms toolset.

The toolset is composed by four major components, all based on docker open platform (*Docker Overview*, 2021; Merkel, 2014), which is a state of the art, well-known, open-source platform for developing, sharing and running

applications as a sandbox service called *containers*, with full support for NVIDIA GPU (CUDA) computing (Luebke, 2008). More information on docker available on supporting information Text S5.

The first component is the *ImageProcessingUtils* docker container (Nodjoumi, 2021a), a jupyter notebook tool developed for resize, crop, remove black borders, tile and convert images from CUB (Anderson Jeff & Deborah Lee Soltesz, 2003), jpeg2000 and GeoTiff file formats to GeoTiff, jpeg and png file formats maintain georeferencing information in file metadata for GeoTiff or in an ancillary world files for jpeg and png.

The second component, is *Labelme* docker container, an open-source tool with graphical user interface for creating segmentation labels (Wada, 2021).

The third component is DeepLandforms docker container which includes two jupyter notebook, both built on top of Detectron2 library, *DeepLandforms-Training* and *DeepLandforms-Segmentation*. More detailed description are provided in supporting information Text S6.

The fourth component is *Tensorboard* docker container, a simple utility for monitoring the training process.

3. Materials and Methods

3.1. Data

The data used in this work are mainly images acquired by image sensors operating in the visible (VIS) and Near InfraRed (NIR) spectrums on board of probes orbiting Mars and the Moon as shown in Table 1.

Orbiter	Target	Instrument	Sensor type	Ground Resolution	Images
Mars Reconnaissance Orbiter (MRO)	Mars	High Resolution Image Science Experiment (HiRISE)	Panchromatic VIS+NIR	Up to .30 m/pixel	~1000

Table 1. The dataset used for training and testing purposes is a combination of three subset samples of global coverage major datasets.

This dataset is composed of images by different instruments and space missions downloaded both as Reduced Data Record (RDR) and Experiment Data Record (EDR) format from public space archives such as PDS Geosciences Node Orbital Data Explorer (ODE) (PDS Geosciences Nodes, 2021). EDR images have been processed initially to produce RDR version using USGS Integrated Software for Imagers and Spectrometers (ISIS) (Laura et al., 2021) and then converted into jpeg2000 (JP2) file format or GeoTiff file format using *ImageProcessingUtils* container.

Computational requirements of Machine Learning and more in particular of Deep Learning architectures for Computer Vision, apart from the complexity of the architecture, are strictly related to image properties, image bands, resolution (size), dataset size, that have a great impact especially during training of the model. On the other hand, the impact on computation and resources during the usage of the pre-trained model is lower. In comparison, the Mars and Moon high-resolution images from HiRISE and LROC respectively, are enormous in terms of data size, reaching easily 50000pixel height resolution at 0.3m/pixel ground resolution (on average). These require a lot more processing in order to make them compatible with Deep Learning tasks or to reduce the computational requirements.

A simple and easy approach would be the direct resize of these images but is not always possible because there is the risk of loose object's unique details or even worse introduce apparent similarity between two different objects.
A better approach is to divide the images into desired resolution tiles, in this case there is no detail loss but the number of images to be filtered out of irrelevant ones and then labeled increases proportionally of image original and desired resolution. E.g., HiRISE PSP_004715_1855_RED image is 30137x76047 pixels, dividing it into ~512x512 pixels tiles results in more than ~8700 tiles. Even tiling into larger tiles is not always a feasible approach. Moreover, such tiling may result in the loss of contextuality of the objects or introduce difficulties during the labeling tasks since the object may result splitted into multiple tiles.
In this situation it is advised to define the requirements of the analysis and evaluate compromises between the approaches of Table 2.

Requirements	**Limits**	**Compromises**	**Approach**
Maintain context	Scaling to very low resolution may lead to huge loss of details	Limit the scaling to maintain discretization capabilities	Scaling approach
Maintain high discretization and avoid object splitting	Larger images produce several tiles proportional to original image and tiles resolution, objects may results split across several tiles	Limit the dimension of the tiles to avoid object splitting and number of tiles low	Tiling approach

Table 2. Comparison between approaches, scaling approach may be better for analysis of features at regional scale, while tilin approach may be preferred for smaller landforms.

In the presented use case, a mixed approach has been used: images spatial resolution have been scaled down to 5 m/pixel, then the resulting images have been sliced into tiles with 1024 pixel max width or height. To achieve these specific tasks, the docker container named ImageProcessingUtils.

3.2. Masks world coordinates

As mentioned in the introduction, all results obtained by Mask-R-CNN are image masks described with pixel coordinates. Therefore it is necessary to convert in world coordinates. This operation has been accomplished by developing a function based on a Python library named Rasterio (Gillies & others, 2021) which contains specific modules for spatial data manipulation by using each image affine transform. See Text S4 and Figure S1 in supporting information.

4. Results

Hereby are described the results obtained after re-training Mask-R-CNN models on a custom dataset of HiRISE images containing pit/skylights landforms.
All the configuration parameters, the components of DeepLandforms, including the descriptions of the data pre-processing and labeling components, the training and inference jupyter notebooks and the types of results obtainable are available in supporting information Text S3, S4, S5, S6, S7, Table S3, S4, S5.

4.1. Pits/Skylight use-case

Despite this toolset is not specific to any kind of landforms, the target used as test landform consist of pits/skylights with a comparison with craters.

Craters are almost circular to elongated depressions caused by an impact of an object. Dimensions may vary a lot across the solar system and are guided by several aspects such as the presence of an atmosphere, the geology of the area, the velocity and trajectory of the object, the gravity of the planet and more. Commonly, they are characterized by a bulged rim, shallow to steep walls, radial eject marks and a small summit at the center (Evans, 2012; Hargitai & Kereszturi, 2015b; Michikami et al., 2014; Mouginis-Mark, 2004). These characteristics are more visible in craters that are newer, larger, or more in general, that were less subject to recent or present erosional processes, e.g. atmospheric ones in the case of Mars. In later stages of erosion and alteration some characteristics tend to be obliterated or smoothed, resulting in morphologies that resemble pits or skylights.

Pit and skylight are depressions of the terrain characterized by an elongated to almost circular shape, flat rims and bottom, walls ranging from almost flat to very steep and in some cases sub-vertical (Cushing et al., 2015; Cushing & Titus, 2010; F. Sauro et al., 2020; U. Sauro, 2016; van der Bogert & Ashley, 2015; Wyrick, 2004). On Earth are commonly caused by the collapse of the top of a subsurface cavity, or by chemical or mechanical erosion of the subsurface sediments, while on other planetary bodies such Mars and the Moon, their formation mechanisms are still debated. As mentioned before, pits and skylights may have different shapes and dimensions on Earth and other planetary bodies (Cushing et al., 2015; Hong et al., 2015; F. Sauro et al., 2020; Sharma & Srivastava, 2021; Whitten & Martin, 2019), yet maintain almost all the characteristics. The classification proposed Figure 4, is an expansion of the classification proposed by Cushing et al (Cushing et al., 2015) and is based only on a qualitative morphological analysis based on visual appearances of the features characteristic of pits and skylight, without taking into account morphometric properties.

Image	ID	Description
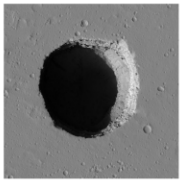	1a	Type 1a – Skylight with possible cave entrance characterized by quasi perfect circular shape, flat rim, no ejecta marks, and almost nonvisible bottom. When visible bottom is present, it is possible to see vertical to overhanging walls by the projected shadows and in some cases piles of debris at the center with conical upward shape. Often found isolated or in proximity of all other types, especially Type-4 and Types-2a-b.
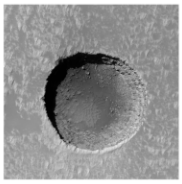	1a	Type 1b – Pit with possible relation to cave entrance and, or lava tube characterized by quasi circular shape, sub-vertical to vertical walls, almost flat rim, no ejecta marks, almost circular shape, and visible bottom. In some cases, it is possible to see circular marks of darker terrain on the floor, near the sub-vertical walls.
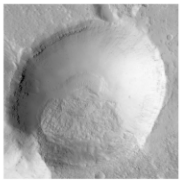	2a	Type 2a – "Bowl" pit with uncertain connection to lava tubes or dikes characterized by a semicircular shape, almost flat rim, no ejecta marks, sloped walls and visible convex bottom. Often isolated or in connection with Type-3
	2b	Type 2b – Pit with uncertain connection to lava tubes or dikes characterized by a semi elliptic shape, almost flat rim, no ejecta marks, sloped walls and visible convex to flat bottom. Often isolated or in connection with Type-3
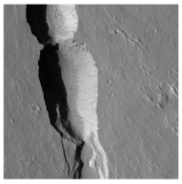	3	Type 3 – Coalescent pits characterized by a mix of characteristics of Type-2a-b. Possible connection to lava tubes or dykes due to the alignment of Type-2a-b.
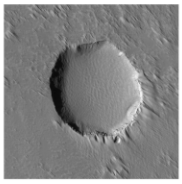	4	Type 4 – Pit with possible connection to lava tubes or dikes due to the alignment of multiple similar shapes, characterized by a semicircular shape, almost flat rim, no ejecta marks, shallow to very shallow depth, sloped to sub-vertical walls and visible flat bottom. Often aligned with other Type-4 or in connection with Type-3 and Type-1a-b, rarely isolated.

Figure 4. Main types of pits/skylights that can be identified on Mars, also used as classes for labeling training dataset, expanded from a previous work (Nodjoumi et al., 2021).

The most consistent and peculiar characteristic among pits/skylights that almost always differ greatly from craters is the presence of a raised rim. As previously mentioned, in craters it's common to find bulge all along the rim, or in a specific direction that usually correspond to the impact trajectory, while rims in pits and skylights are almost

completely absent or associated with previously existent landforms that can be visible also in the nearby of the pits and skylights.

The best method to evaluate the differences between pit and crater rims, is to manually plot and evaluate Digital Terrain Model (DTM) profiles but, since in most cases DTMs are not always available, it is possible to evaluate them by plotting a profile along the maximum illumination direction of visible images, obtaining a pixel intensity profile that correspond to brightness levels of the pixels, with digital number (DN) with values ranging from 0 (black) and 255 (white). Although 16-bit images could provide major details in the shadowed areas, 8-bit images were preferred as their 16-bit counterpart increases computational requirements dramatically and are not completely implemented yet in common Deep Learning techniques for object detection and segmentation. This method is an approximated and indirect estimation of the orientation of the surface and assumes that the substrate is almost homogeneous. Low brightness values correspond to shadowed areas with solar incidence angle near 90°, while high brightness values correspond to lower solar incidence angle. The solar incidence angle is the angle between the solar rays and the normal on a surface and has an absolute range between 0° and 90° (Kalogirou, 2009). This approach is also the core of other works that have the same aim of identifying pits on other Solar System rocky bodies (Lohse et al., 2006; Robinson et al., 2017).

Craters brightness profiles can be created using QGIS profile plugin as shown in Figure 5.

Profiles can be divided in six main sections, in which there are almost two pairs of paired high peak-bottom brightness sections corresponding to the area of morphological bulge's illuminated and shadowed faces. Those sections can be described as follows:

1) Pre-rim: brightness is almost uniform and visually similar to the surroundings of the landform.
2) 1st Sun-faced rim: inner side of the pit exposed to direct sun's rays opposite of section 2. Divided in two sub-sections:
    a. Lower ramp: brightness increases gradually towards the rim with values up to those of section 1. Not always present in conjunction with 3b.
    b. Higher ramp: brightness increases abruptly, with values equal or major than those of section 1, meaning that the solar incidence angle is decreasing. Not always present in conjunction with 3a.
3) 1st anti-solar rim: side of 1st bulge not exposed directly to sunlight, brightness decreases with values lower than section 1, depending on inclination of the internal bulge and the landforms. Divided in two subsections:
    a. Penumbra: brightness decreases uniformly. Non always present in conjunction with 3b.
    b. Umbra: brightness decreases abruptly, usually completely dark or with DN values near to 0, those values may slightly increase moving near the next rim or increase abruptly. Non always present in conjunction with 3a.
4) 2nd sun-faced rim: side of the 2nd bulge, divided in 4a and 4b, similarly to section 2a and 2b.
5) 2nd anti-solar rim: side of the 2nd bulge, divided in 5a and 5b, similarly to section 3a and 3b.

Post-bulge area: brightness increases up to levels similar to section 1.

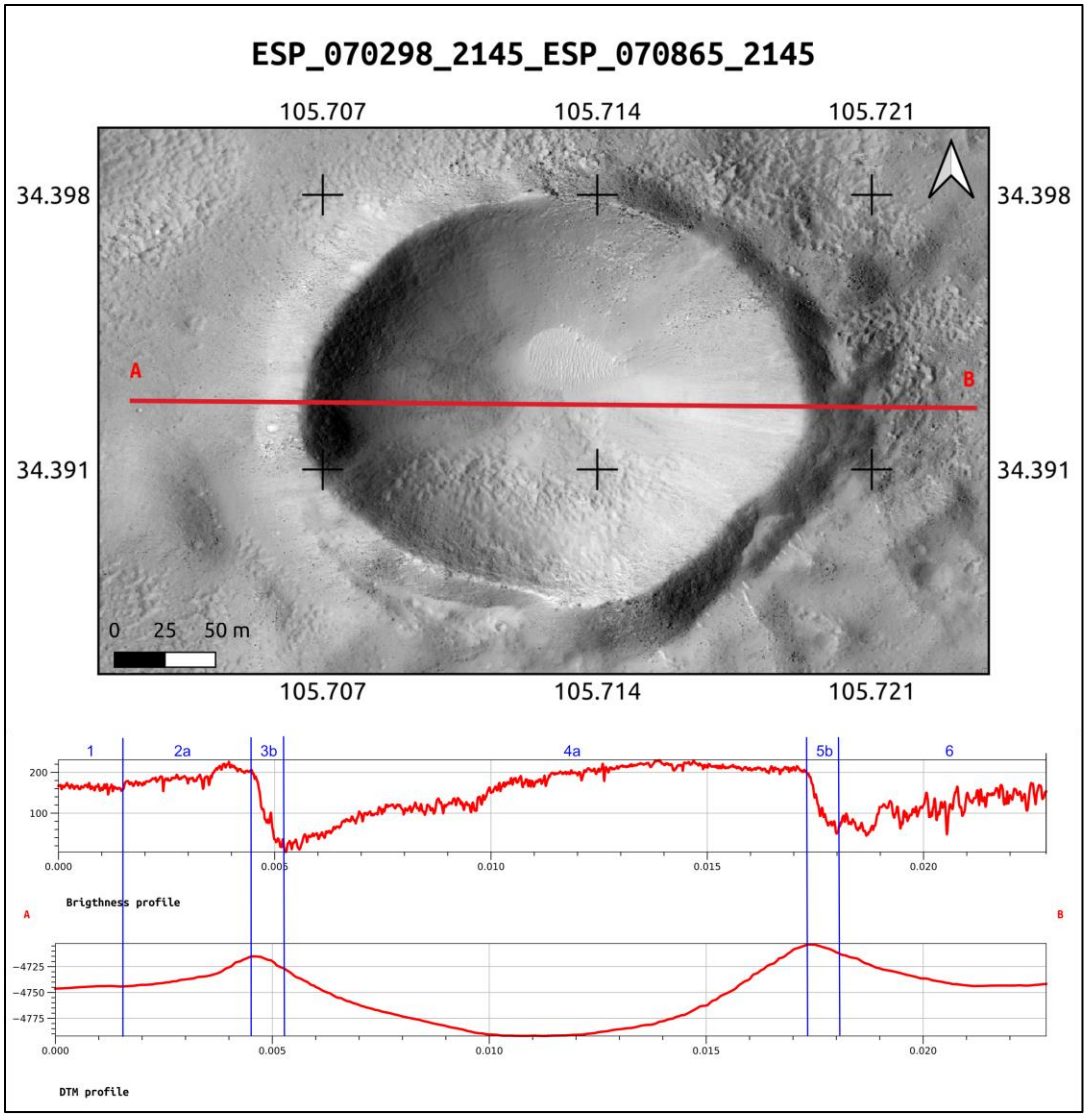

Figure 5. Comparison of brightness and DTM profiles for a crater on ESP_070298-ESP_070865 stereo pair, red channel. In blue, an attempt to identify the correspondence of the brightness sections on a DTM derived from photogrammetry of HiRISE stereo pair.

Pits/Skylights brightness profiles, created using QGIS profile plugin, as shown in Figure 6. Additional example in Figure S3 in supporting information.

The profiles are divided in 4 main sections, described as follows*:*

1) Pre-pit: brightness is almost uniform with values similar to the surroundings of the landform.
2) Funnel: brightness decreases with values lower than section 1, depending on inclination of the morphological slope of the surfaces. Divided in two sub-sections:
   a) Penumbra: brightness decreases uniformly. In some cases, brightness may drop abruptly then remaining almost constant or decreasing uniformly with values always higher than DN 0. Non always present in conjunction with 2b.

b) Umbra: brightness decreases abruptly, usually completely dark or with DN values near to 0, those values may slightly increase moving near the next rim or increase abruptly. Non always present in conjunction with 2a.

3) Sun-faced rim: inner side of the pit exposed to direct sun's rays opposite of section 2. Divided in two sub-sections:

a) Lower ramp: brightness increases gradually towards the rim with values up to those of section 1. Not always present in conjunction with 3b.

b) Higher ramp: brightness increases abruptly, with values equal or major than those of section 1, meaning that the solar incidence angle is decreasing. Not always present in conjunction with 3a.

4) Post-pit area: intensity levels become similar or identical to those of section 1.

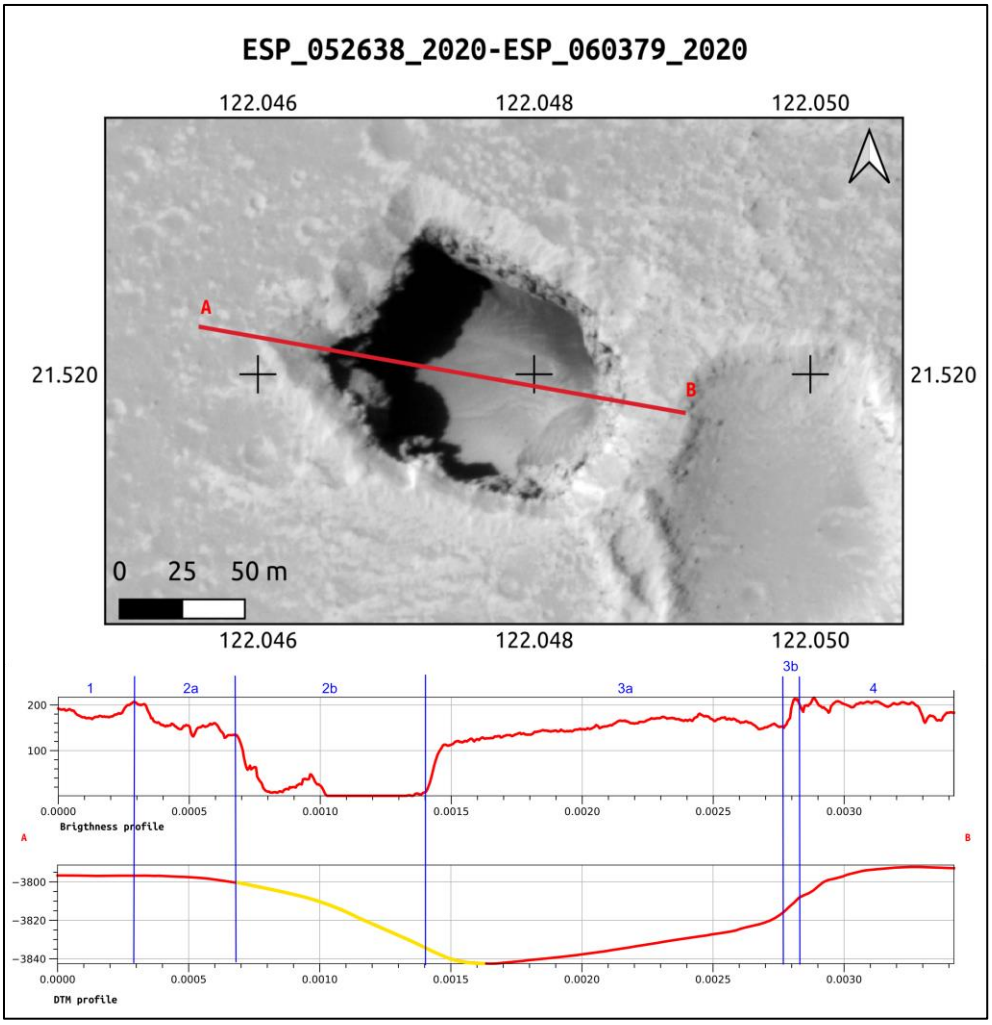

Figure 6. Comparison of brightness and DTM profiles for a Type-1 on ESP_052638_2020-ESP_060379_2020 stereo pair, red channel. In blue, an attempt to identify the correspondence of the brightness sections on a DTM derived from photogrammetry of HiRISE stereo pair. In yellow, the portion of the DTM profile interpolated by the Socet Set ((c) BAE Systems) software. The interpolation is due to lack of usable data in both the images processed using photogrammetry (HiRISE | About HiRISE Digital Terrain Models, 2021).

In order to validate all the packages, tools and the complete workflow, an intensive test has been performed on the above-mentioned pit, skylights landforms, including a generic set of craters for references and for testing the capability to discriminate those whose appearance resemble some types of pits.

The dataset consists of 89 HiRISE RDR red channel images, see supporting information Table S5. The use of only red channel images is due to the swath of 6 km cross-orbit and 20 km along-orbit at a nominal 300 km nominal orbit. In comparison the Blue-Green and NIR images have a swath resolution of 1.2 km cross-orbit.

Those image have been processed using ImageProcessingUtils (Nodjoumi, 2021a) to convert from jpeg2000 file format (JP2) to GeoTiff and then resized to a common 5 m/pixel cell size, and tiled into more usable files with the largest side up to maximum 1024 pixel.

All resulting images have been manually examined to filter out those which did not contain any landform relevant for the labeling steps, obtaining 152 images containing at least one type of landform.

Then, all the images have been ingested into LabelMe to annotate all the pits, the skylights and some representative craters following the classification showed in Figure 4. At the end of the labeling task, it emerged that the obtained labels were unbalanced, meaning that the dataset does not contain an almost equal number of each class.

Since the collection and processing of newer images containing more landforms of the unbalanced classes was not feasible at the time of analysis, a simpler approach was chosen and consist of a reduction of the classes by grouping into similar ones, doing so resulted in only four classes, Type-1, containing -1a and -1b, Type-2, containing -2a and -2b, Type-3, Type-4.

After concluding the dataset preparation, several training sessions were performed using DeepLandforms-training notebook, with different parameters and *mask_rcnn_R_50_FPN_3x* as model configuration; to evaluate the stability and scalability and the performance of the tool with the dataset on two different computers.

According to Detectron2's model zoo (Y. Wu et al., 2019b), which is a large collection of model configurations and their corresponding pre-trained models and baseline performance values, mask_rcnn_R_50_FPN_3x model configuration is reported to have the best-balanced results/training requirements ratio, see supporting information Text S7 for details on the model configuration. The ranges of the main training parameters are summarized in supporting information Table S3.

All the training sessions have been monitored using tensorboard to evaluate the progression and the performance of the trainings and resulted in promising results, despite the small dimensions of the datasets and the not optimized training parameters. As it is possible to see in supporting information Figure S11, the accuracy for bounding boxes and masks reached more than 0.99 after 5000 epochs, with very low ratios of false negatives and false positives and final mean Average Precision values shown in supporting information Table S4 and Figure S9-S10.

Those values are mostly in accordance with the average values of the architecture's benchmarks (Y. Wu et al., 2019b), the low values obtained for craters and Type-4 are mainly caused by the low quantities of respective labeled data and the similarities that may occur in some landforms.

The obtained model was then used to inference the valid dataset, and then the results were loaded into LabelMe to check if the labeled objects are detected and labeled correctly as shown in Figure 7.

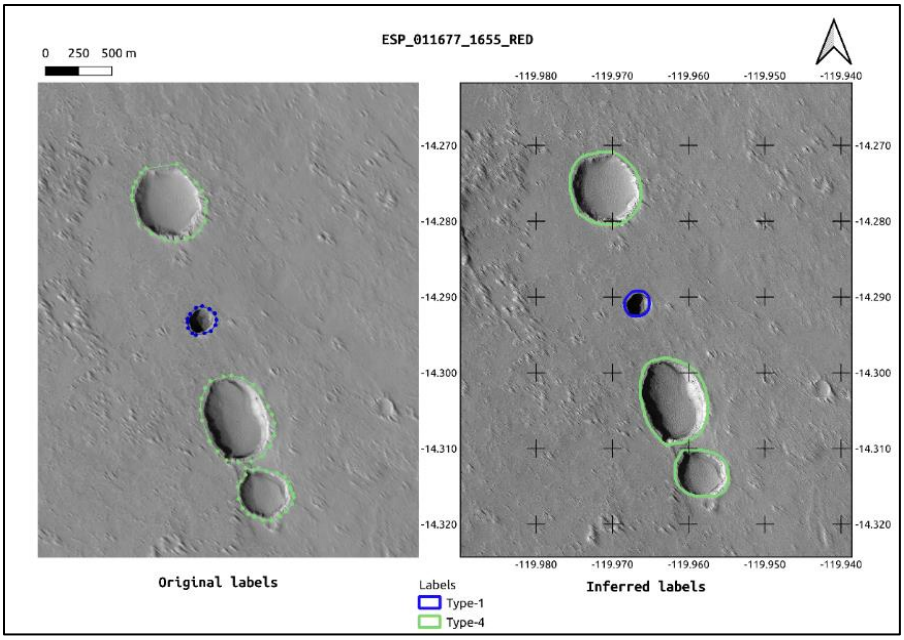

Figure 7. Comparison between ground truth labeled image used in training (left) and inferred labeled image (right). The major difference is in the density of the points of the shape, where in the inferred image are way denser than those of the ground truth.

Then the model was used on a partially new set of HiRISE RDR red channel images, in a limited area over the Tharsis Region on Mars.

This region has its central coordinates at 0°N 260°E and was selected three of the largest shield volcanoes in the Solar System are located here, Arsia Mons, Pavonis Mons and Ascreus Mons, moreover in its western area is located the tallest shield volcano in the Solar System, the Olympus Mons. Considering the presence of these large shield volcanoes this region and thus possible intact lava tubes, is the best candidate region to look for possible cave entrances. A previous work by Cushing et al. (Cushing, 2017), identified and published a database containing thousands of pit/skylights landforms, by analyzing manually several Context Camera (CTX) and HiRISE imagery.

This database was used as a control data for all the analyses performed in this and the previous work (Nodjoumi et al., 2021).

The results of the inference performed using DeepLandforms, contained in a geopackage file, was imported in QGIS software, to better inspect the results obtained as shown in Figure 8.

It is possible to see multiple mis-aligned detections of the same landform, this is not properly an error since and is due to presence of two images that are originally acquired from different orbit and not perfectly coregistered or granules relatives to a stereo pair, thus the slightly misalignment, which does not affect the manual validation. To avoid these occurrences, it is necessary to manually check the working dataset for duplicates or use only coregistered data.

In Figure 8, is presented an example of the obtained results, compared to the entries of the MGC^3 database and theresults obtained in the DeepLandforms-YOLOv5 object detection work, showing a very good detection and segmentation of the trained landforms. Moreover, it is possible to see the advantages of the approach proposed in this work. Providing polygon geometries as results, could greatly improve the mapping of specific landforms, especially

when looking for unknown occurrences on a wide dataset. More examples are available in Supporting information Figures S4 to S8.

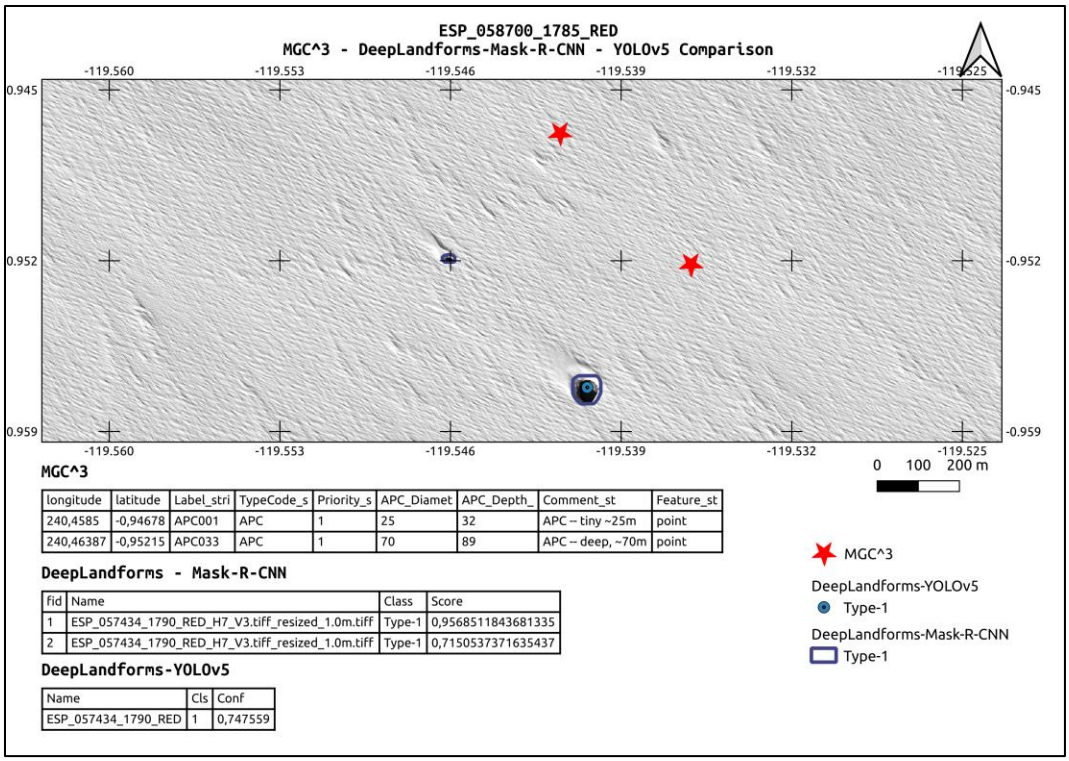

MGC^3

longitude	latitude	Label_stri	TypeCode_s	Priority_s	APC_Diamet	APC_Depth_	Comment_st	Feature_st
240,4585	-0,94678	APC001	APC	1	25	32	APC – tiny ~25m	point
240,46387	-0,95215	APC033	APC	1	70	89	APC – deep, ~70m	point

DeepLandforms - Mask-R-CNN

fid	Name	Class	Score
1	ESP_057434_1790_RED_H7_V3.tiff_resized_1.0m.tiff	Type-1	0,9568511843681335
2	ESP_057434_1790_RED_H7_V3.tiff_resized_1.0m.tiff	Type-1	0,7150537371635437

DeepLandforms-YOLOv5

Name	Cls	Conf
ESP_057434_1790_RED	1	0,747559

Figure 8. Example of detection on HiRISE Red channel image and comparison between MGC^3, DeepLandforms-YOLOv5 object detection and DeepLandforms-Mask-R-CNN instance segmentation. Tables show attributes of fields in the shapefiles. The offset of MGC^3 points is probably caused by the coordinate conversion of the source MGC^3 csv file into shapefile.

Notice that in all the presented images, there is a misalignment between the MGC^3 points and the HiRISE or CTX Images. The cause of this discrepancy has not been identified yet but is probably due to a different reference system used by the authors of MGC^3 or introduced during the conversion from the source MGC^3 csv file to the shapefile file format.

5. Discussion

In this work, are presented the mapping results of skylight, pit and pit chains automated mapping using only DeepLandforms, a novel comprehensive toolset based on Deep Learning Computer Vision for object detection and segmentation.

Skylight, pits and pit chains are an extremely interesting type of landforms that can be observed on almost all rocky planets and moons of the Solar System.

Formation mechanisms are commonly related to volcanic and tectonic processes but are still debated, moreover it is still not clear whether such formation mechanisms are the same on all the planetary bodies in which those landforms

433 are observed, especially since there are very similar and common morphological characteristics among all
434 observations. If it is the case of common formation mechanisms, this implies that there should be shared geological
435 properties and settings among those bodies, thus common geological history.
436 Further on, skylights and some pits may have access to caves as observed on Earth analogues, and hypothesized on
437 Mars and the Moon (Hong et al., 2015), such those found on large shield volcanoes (Léveillé & Datta, 2010; F. Sauro
438 et al., 2020). Presence of accessible caves on other planets and moons has an huge importance for space exploration
439 since those cave may contain traces of life, both past and potentially present, as some extremophile bacteria and other
440 smaller life-form may have found shelter from harsh surface condition and cosmic radiations (NASA, 2021).
441 Moreover, caves are considered as good candidates for future human habitation outposts (Cushing & Titus, 2010;
442 Pipan & Culver, 2019), and also are an excellent window on the subsurface structure, thus providing valuable
443 information for understanding the geological settings and evolution of the area and potential direct access to mineral
444 resources (Blamont, 2014).
445 To explore the above-mentioned targets and objectives, is necessary an accurate and global scale mapping of skylight,
446 pit and pit chains, in order to better understand the spatial distribution of such landforms and correlate their presence
447 with other geological and non-geological features and settings.
448 For instance, since pit chains may be related to the presence of lava tubes or dykes (Ferrill et al., 2011; Whitten &
449 Martin, 2019; Wyrick, 2004), mapping pits could lead to new understandings of lava tube distribution, thus to better
450 knowledge of volcanic processes involved, even across planets and moons. Isolated pits with no surrounding other
451 morphological evidence may indicate the presence of a deep buried lava tube or cavity originating from other
452 processes.
453 It is also possible to compare the distribution of such landforms with structural maps or other features that may be
454 interconnected (Ferrill et al., 2004, 2011).
455 Another advantage is connected to the planetary human mission planning, since the availability of geomorphological
456 maps, even if not at highest resolution possible, may lead to the identification of better scientific targets or path
457 planning in case of rovers.
458 An automated or semi-automated approach as the one proposed in this work, in comparison to the manual mapping,
459 may be a game-changer, providing robust processing workflows for generate high-end data in compliance with the
460 OGC standards, for map productions at planetary scale, with the enormous advantage of relaying the most time-
461 consuming task of data pre-process and first analysis to computer time instead of human-time.
462 Presented results are very promising, despite some issues that must be considered.
463 Despite the very good correspondence of the shapes of the detections and the proper real shape, some refinements
464 may be necessary, as some landforms are not detected at all, or in some cases wrongly classified.
465 Moreover, in some cases there is a detection ambiguity, in which some resulting shapes appear doubled, non-unique
466 or mis-aligned, due to the analysis performed on not co-registered images of the same area, as shown in Figures S4
467 and S8 in supporting information.
468 Poor labeling and bad train configuration parameters can also lead to models not suitable for deployment in production
469 uses, or completely unreliable.

To improve those results the first step is to increase the quality and quantity of the training dataset, then tuning the configurations of the architecture used and eventually try different networks that may be more adequate to different landforms.

The analysis presented in this work, if expanded to a large dataset, may greatly expand the knowledge of the spatial distribution of skylights, pits, and pit chains, including those already known and described, providing a detailed wide map that can be further integrated with morphometric analyses.

All the main blocks of the workflow presented in Figure 3 were performed exclusively on DeepLandforms *'s* modules, data collection was performed using NASA-PDS data archive web services, and results evaluation and comparison was performed using QGIS software.

The quality of the obtained results can be improved by increasing the amount of images in the initial dataset and their spatial resolution. This will provide more labels to the model that will better learn the differences among all the studied objects. Hyperparameters of the used network can be also tuned to achieve better results. This applies not only to this specific case but to every object detection and segmentation problem.

The major limit of those automated approaches resides in the context-unawareness, meaning that when performing the analyses, all the networks are not performing a context-aware analysis in addition to the object detection and identification. This means that at the time of writing there are not yet architectures, for this kind of tasks, that evaluate the surrounding, the context, of a detection to optimize the identification of the objects present in the area.

Recently there are architectures that are capable of such additional analyses, called *Liquid Time-constant Networks* (Hasani et al., 2020) but are still under development.

6. Conclusions

The advantages and improvements in data analysis provided by machine learning are undoubtful and constantly expanding in more and more sectors especially in remote sensing of Earth and Space. With an exponential amount of fast-growing available datasets, newer and faster methods are necessary to perform a continuous stream of analyses, and with a plethora of publications, works, architectures and unconnected tools available, that are mainly *accessible* by everyone, albeit not *usable* by not insiders, is also necessary to make those available for the wider audience, especially those who are involved in the analyses of data but are not specialized in the machine learning.

In these settings, DeepLandforms, presented in this work, may be a forerunner, a tentative to lead an easier approach well suitable both for first-time users and advanced users.

The major advantages and disadvantages are summarized in Table 3:

Advantages	**Disadvantages**
Almost ready-to-use	Not compatible to every platform
Semi-automated approach	Require intensive user supervision in the initial phase and during preliminary evaluation
Large data volume processing capabilities	Depends on the machine in which is running
Possibly to use results for further correlation with other data	
Wide adaptability to different landforms	May not be compatible with every landform type, depending on the training data

Table 3. Tabulated assets and liabilities of the toolset presented in this work.

6.1. Further development

Further development includes implementation of sliding window to improve further the segmentation of large images without pre-tiling them, the integration with GIS statistics such as the parametrization of the detected shapes, including cross-analysis of different data types such as Digital Terrain Models (DTM) in order to improve the quality of the results including eventually volume estimation, or integration with hyperspectral data to retrieve a mineral composition of the surface.

Another development could integrate the workflow with the shape-from-shading technique (Alexandrov & Beyer, 2018; Lohse et al., 2006; Micheletti et al., 2015) in order to extract depth and thus volume information where DTMs are not available.

Moreover, this toolset is not specific to any planetary body nor specific landforms, thus is compatible with every planet or moon imagery, if provided images are georeferenced and the corresponding reference system is passed to the tool.

Acknowledgments: The authors declare no conflicts of interest.

Funding: This study is within the Europlanet 2024 RI and EXPLORE project, and it has received funding from the European Union's Horizon 2020 research and innovation programme under grant agreement No 871149 and No 101004214.

Data Availability Statement:

Open Research

The original data used for this study are available at publicly data archive NASA PDS Geoscience Node Orbital Data Explorer (ODE) (PDS Geosciences Nodes, 2021).

Datasets for this research are available in these in-text data citation references: (Nodjoumi, 2021b) with license GPLv2+ and available at: https://doi.org/10.5281/zenodo.5734912

Software for this research is available in these in-text data citation references: (Nodjoumi, 2021c) with license GPLv2+ and available at: https://doi.org/10.5281/zenodo.5734621

All base images of the figures have been prepared using QGIS software 3.16 LTS and then processed with Affinity Publisher 1.1.

References

Acharya, G., De Smedt, F., & Long, N. T. (2006). Assessing landslide hazard in GIS: A case study from Rasuwa, Nepal. *Bulletin of Engineering Geology and the Environment*, *65*(1), 99–107. https://doi.org/10.1007/s10064-005-0025-y

Alexandrov, O., & Beyer, R. A. (2018). Multiview Shape-From-Shading for Planetary Images. *Earth and Space Science*, *5*(10), 652–666. https://doi.org/10.1029/2018EA000390

Allemand, P., Delacourt, C., Gasperini, D., Kasperski, J., & Pothérat, P. (2011). Thirty Years of Evolution of the Sedrun Landslide (Swisserland) from Multitemporal Orthorectified Aerial Images, Differential Digital Terrain Models and Field Data. *International Journal of Remote Sensing Applications*, *5*, 7.

Alonso, E. E., Pinyol, N. M., & Puzrin, A. M. (2010). Catastrophic Slide: Vaiont Landslide, Italy. In E. E. Alonso, N. M. Pinyol, & A. M. Puzrin, *Geomechanics of Failures. Advanced Topics* (pp. 33–81). Springer Netherlands. https://doi.org/10.1007/978-90-481-3538-7_2

Anderson Jeff & Deborah Lee Soltesz. (2003, June 11). *USGS Isis: Logical Cube Format Guide*. Https://Isis.Astrogeology.Usgs.Gov/. https://isis.astrogeology.usgs.gov/documents/LogicalCubeFormatGuide/LogicalCubeFormatGuide.html

Aye, K.-M., Schwamb, M. E., Portyankina, G., Hansen, C. J., McMaster, A., Miller, G. R. M., Carstensen, B., Snyder, C., Parrish, M., Lynn, S., Mai, C., Miller, D., Simpson, R. J., & Smith, A. M. (2019). Planet Four: Probing springtime winds on Mars by mapping the southern polar CO2 jet deposits. *Icarus*, *319*, 558–598. https://doi.org/10.1016/j.icarus.2018.08.018

Bardabelias, N., Holt, J., & Christoffersen, M. (2020). Potential Detection of Martian Lava Tubes from Mars Global Cave Candidate Catalog Skylight Locations Using SHARAD. *3rd International Planetary Caves Conference*, *2197*, 1068.

Barlow, N. G., Ferguson, S. N., Horstman, R. M., & Maine, A. (2017). Comparison of central pit craters on Mars, Mercury, Ganymede, and the Saturnian satellites. *Meteoritics & Planetary Science*, *52*(7), 1371–1387. https://doi.org/10.1111/maps.12857

Barrett, A. M., Balme, M. R., Woods, M., Karachalios, S., Petrocelli, D., Joudrier, L., & Sefton-Nash, E. (2022). NOAH-H, a deep-learning, terrain classification system for Mars: Results for the ExoMars Rover candidate landing sites. *Icarus*, *371*, 114701. https://doi.org/10.1016/j.icarus.2021.114701

Benedix, G. K., Lagain, A., Chai, K., Meka, S., Anderson, S., Norman, C., Bland, P. A., Paxman, J., Towner, M. C., & Tan, T. (2020). Deriving Surface Ages on Mars Using Automated Crater Counting. *Earth and Space Science*, *7*(3). https://doi.org/10.1029/2019EA001005

559 Blamont, J. (2014). A roadmap to cave dwelling on the Moon and Mars. *Advances in Space Research*, *54*(10),
560 2140–2149. https://doi.org/10.1016/j.asr.2014.08.019
561 Bridge, J., & Demicco, R. (2008). *Earth Surface Processes, Landforms and Sediment Deposits*. 835.
562 Brierley, G., Fryirs, K., Reid, H., & Williams, R. (2021). The dark art of interpretation in geomorphology.
563 *Geomorphology*, *390*, 107870. https://doi.org/10.1016/j.geomorph.2021.107870
564 Brust, C. A., Käding, C., & Denzler, J. (2019). Active learning for deep object detection. *VISIGRAPP 2019 -*
565 *Proceedings of the 14th International Joint Conference on Computer Vision, Imaging and Computer*
566 *Graphics Theory and Applications*, *5*, 181–190. https://doi.org/10.5220/0007248601810190
567 Cahalan, M. D., & Milewski, A. M. (2018). Sinkhole formation mechanisms and geostatistical-based prediction
568 analysis in a mantled karst terrain. *CATENA*, *165*, 333–344. https://doi.org/10.1016/j.catena.2018.02.010
569 Chappaz, L., Sood, R., Melosh, H. J., Howell, K. C., Blair, D. M., Milbury, C., & Zuber, M. T. (2017). Evidence of
570 large empty lava tubes on the Moon using GRAIL gravity: Evidence of Lunar Lava Tubes From GRAIL.
571 *Geophysical Research Letters*, *44*(1), 105–112. https://doi.org/10.1002/2016GL071588
572 Chen, M., Lei, M., Liu, D., Zhou, Y., Zhao, H., & Qian, K. (2017). Morphological Features-Based Descriptive Index
573 System for Lunar Impact Craters. *ISPRS International Journal of Geo-Information*, *7*(1), 5.
574 https://doi.org/10.3390/ijgi7010005
575 Cruikshank, D. P., & Wood, C. A. (1972). Lunar rilles and Hawaiian volcanic features: Possible analogues. *The*
576 *Moon*, *3*(4), 412–447. https://doi.org/10.1007/BF00562463
577 Cushing, G. E. (2017). Mars Global Cave Candidate Catalog (MGC3)[abstract 3708]. *Astrobiology Science*
578 *Conference, Lunar and Planetary Institute, Houston. Available Online at Https://Www. Hou. Usra.*
579 *Edu/Meetings/Abscicon2017/Pdf/3708. Pdf*.
580 Cushing, G. E., Okubo, C. H., & Titus, T. N. (2015). Atypical pit craters on Mars: New insights from THEMIS,
581 CTX, and HiRISE observations: ATYPICAL PIT CRATERS ON MARS. *Journal of Geophysical*
582 *Research: Planets*, *120*(6), 1023–1043. https://doi.org/10.1002/2014JE004735
583 Cushing, G. E., & Titus, T. N. (2010). Caves on Mars: Candidate Sites for Astrobiological Exploration.
584 *Astrobiology Science Conference*, *2010*, 2–3.
585 Cushing, G. E., Titus, T. N., Wynne, J. J., & Christensen, P. R. (2007). THEMIS observes possible cave skylights
586 on Mars. *Geophysical Research Letters*, *34*(17), L17201. https://doi.org/10.1029/2007GL030709

De Blasio, F. V. (2011). Landslides in Valles Marineris (Mars): A possible role of basal lubrication by sub-surface ice. *Planetary and Space Science*, *59*(13), 1384–1392. https://doi.org/10.1016/J.PSS.2011.04.015

Díaz Michelena, M., Kilian, R., Baeza, O., Rios, F., Rivero, M. Á., Mesa, J. L., González, V., Ordoñez, A. A., Langlais, B., Rocca, M. C. L., & Acevedo, R. D. (2020). The formation of a giant collapse caprock sinkhole on the Barda Negra plateau basalts (Argentina): Magnetic, mineralogical and morphostructural evidences. *Geomorphology*, *367*, 107297. https://doi.org/10.1016/j.geomorph.2020.107297

DiPietro, J. A. (2013). The Tortoise and the Hare. *Landscape Evolution in the United States*, 3–14. https://doi.org/10.1016/B978-0-12-397799-1.00001-4

Docker overview. (2021, November 12). Docker Documentation. https://docs.docker.com/get-started/overview/

Duhart, P., Sepúlveda, V., Garrido, N., Mella, M., Quiroz, D., Fernández, J., Moreno, H., & Hermosilla, G. (2019). *The Santa Lucía landslide disaster, Chaitén-Chile: Origin and effects*. 9.

Dundar, M., Ehlmann, B. L., & Leask, E. K. (2019). Machine-Learning-Driven New Geologic Discoveries at Mars Rover Landing Sites: Jezero and NE Syrtis. *ArXiv:1909.02387 [Astro-Ph, Stat]*. http://arxiv.org/abs/1909.02387

ESRI technical document. (1998). *ESRI Shapefile Technical Description*. https://www.esri.com/content/dam/esrisites/sitecore-archive/Files/Pdfs/library/whitepapers/pdfs/shapefile.pdf. https://www.esri.com/content/dam/esrisites/sitecore-archive/Files/Pdfs/library/whitepapers/pdfs/shapefile.pdf

Evans, I. S. (2012). Geomorphometry and landform mapping: What is a landform? *Geomorphology*, *137*(1), 94–106. https://doi.org/10.1016/j.geomorph.2010.09.029

Ferrill, D. A., Wyrick, D. Y., Morris, A. P., Sims, D. W., & Franklin, N. M. (2004). Dilational fault slip and pit chain formation on Mars. *GSA Today*, *14*(10), 4. https://doi.org/10.1130/1052-5173(2004)014<4:DFSAPC>2.0.CO;2

Ferrill, D. A., Wyrick, D. Y., & Smart, K. J. (2011). Coseismic, dilational-fault and extension-fracture related pit chain formation in Iceland: Analog for pit chains on Mars. *Lithosphere*, *3*(2), 133–142. https://doi.org/10.1130/L123.1

Geomorphological mapping. (2013). *Geomorphological Techniques*, 10.

615 Ghorbanzadeh, O., Blaschke, T., Gholamnia, K., Meena, S., Tiede, D., & Aryal, J. (2019). Evaluation of Different
616 Machine Learning Methods and Deep-Learning Convolutional Neural Networks for Landslide Detection.
617 *Remote Sensing*, *11*(2), 196. https://doi.org/10.3390/rs11020196
618 Gillies, S. & others. (2021). *Rasterio: Geospatial raster I/O for Python programmers*. Mapbox.
619 https://github.com/rasterio/rasterio
620 Grace, R. K., Anitha, J., Sivaramakrishnan, R., & Sivakumari, M. S. S. (2021). *Crop and Weed Classification Using*
621 *Deep Learning*. 4.
622 Grant, J. A., Irwin, R. P., Grotzinger, J. P., Milliken, R. E., Tornabene, L. L., McEwen, A. S., Weitz, C. M.,
623 Squyres, S. W., Glotch, T. D., & Thomson, B. J. (2008). HiRISE imaging of impact megabreccia and sub-
624 meter aqueous strata in Holden Crater, Mars. *Geology*, *36*(3), 195. https://doi.org/10.1130/G24340A.1
625 Greeley, R. (1971). Lava tubes and channels in the lunar Marius Hills. *The Moon*, *3*(3), 289–314.
626 https://doi.org/10.1007/BF00561842
627 Guallini, L., Rossi, A. P., Forget, F., Marinangeli, L., Lauro, S. E., Pettinelli, E., Seu, R., & Thomas, N. (2018).
628 Regional stratigraphy of the south polar layered deposits (Promethei Lingula, Mars): "Discontinuity-
629 bounded" units in images and radargrams. *Icarus*, *308*, 76–107.
630 https://doi.org/10.1016/j.icarus.2017.08.030
631 Guimpier, A., Conway, S. J., Mangeney, A., Lucas, A., Mangold, N., Peruzzetto, M., Pajola, M., Lucchetti, A.,
632 Munaretto, G., Sæmundsson, T., Johnsson, A., Le Deit, L., Grindrod, P., Davis, J., Thomas, N., &
633 Cremonese, G. (2021). Dynamics of recent landslides (<20 My) on Mars: Insights from high-resolution
634 topography on Earth and Mars and numerical modelling. *Planetary and Space Science*, *206*(July), 105303.
635 https://doi.org/10.1016/j.pss.2021.105303
636 Gutiérrez, F., Guerrero, J., & Lucha, P. (2008). A genetic classification of sinkholes illustrated from evaporite
637 paleokarst exposures in Spain. *Environmental Geology*, *53*(5), 993–1006. https://doi.org/10.1007/s00254-
638 007-0727-5
639 Hare, T. M., Rossi, A. P., Frigeri, A., & Marmo, C. (2018). Interoperability in planetary research for geospatial data
640 analysis. *Planetary and Space Science*, *150*, 36–42. https://doi.org/10.1016/j.pss.2017.04.004
641 Hargitai, H., & Kereszturi, Á. (2015a). *Encyclopedia of planetary landforms*. Springer.

642 Hargitai, H., & Kereszturi, Á. (Eds.). (2015b). Impact Crater. In *Encyclopedia of Planetary Landforms* (pp. 972–
643 972). Springer New York. https://doi.org/10.1007/978-1-4614-3134-3_100204
644 Haruyama, J., Hioki, K., Shirao, M., Morota, T., Hiesinger, H., van der Bogert, C. H., Miyamoto, H., Iwasaki, A.,
645 Yokota, Y., Ohtake, M., Matsunaga, T., Hara, S., Nakanotani, S., & Pieters, C. M. (2009). Possible lunar
646 lava tube skylight observed by SELENE cameras. *Geophysical Research Letters*, *36*(21), L21206.
647 https://doi.org/10.1029/2009GL040635
648 Hasani, R., Lechner, M., Amini, A., Rus, D., & Grosu, R. (2020). Liquid Time-constant Networks.
649 *ArXiv:2006.04439 [Cs, Stat]*. http://arxiv.org/abs/2006.04439
650 He, K., Gkioxari, G., Dollár, P., & Girshick, R. (2018). Mask R-CNN. *ArXiv:1703.06870 [Cs]*.
651 http://arxiv.org/abs/1703.06870
652 Hipperson, M., Waldmann, I., Grindrod, P., & Nikolaou, N. (2020). *Mapping Mineralogical Distributions on Mars*
653 *with Unsupervised Machine Learning* [Other]. oral. https://doi.org/10.5194/epsc2020-773
654 *HiRISE | About HiRISE Digital Terrain Models*. (2021). https://www.uahirise.org/dtm/about.php
655 Hoeser, T., & Kuenzer, C. (2020). Object detection and image segmentation with deep learning on Earth observation
656 data: A review-part I: Evolution and recent trends. *Remote Sensing*, *12*(10).
657 https://doi.org/10.3390/rs12101667
658 Hong, I. S., Yi, Y., Yu, J., & Haruyama, J. (2015). 3D modeling of lacus mortis pit crater with presumed interior
659 tube structure. *Journal of Astronomy and Space Sciences*, *32*(2), 113–120.
660 https://doi.org/10.5140/JASS.2015.32.2.113
661 Hooper, D. M., & Smart, K. J. (2013). Characterization of Landslides on Mars and Implications for Possible Failure
662 Mechanisms. *Lunar and Planetary Science Conference*, *1719*, 1795.
663 Horvath, T., Hayne, P., & Paige, D. (2020). Thermal Environments and Illumination in Lunar Pits and Lava Tubes.
664 *Lunar and Planetary Science Conference*, *2326*, 1729.
665 Hu, Y., Xiao, J., Liu, L., Zhang, L., & Wang, Y. (2021). Detection of Small Impact Craters via Semantic
666 Segmenting Lunar Point Clouds Using Deep Learning Network. *Remote Sensing*, *13*(9), 1826.
667 https://doi.org/10.3390/rs13091826
668 Hungr, O., Leroueil, S., & Picarelli, L. (2014). The Varnes classification of landslide types, an update. *Landslides*,
669 *11*(2), 167–194. https://doi.org/10.1007/s10346-013-0436-y

James, L. A., Harden, C. P., & Clague, J. J. (2013). 13.1 Geomorphology of Human Disturbances, Climate Change, and Hazards. In *Treatise on Geomorphology* (pp. 1–13). Elsevier. https://doi.org/10.1016/B978-0-12-374739-6.00339-0

Jiang, F. (2020). Criteria of sinkhole formation in soils from physical models. *Bulletin of Engineering Geology and the Environment*, *79*(7), 3833–3841. https://doi.org/10.1007/s10064-020-01768-0

Kaku, T., Haruyama, J., Miyake, W., Kumamoto, A., Ishiyama, K., Nishibori, T., Yamamoto, K., Crites, S. T., Michikami, T., Yokota, Y., Sood, R., Melosh, H. J., Chappaz, L., & Howell, K. C. (2017). Detection of Intact Lava Tubes at Marius Hills on the Moon by SELENE (Kaguya) Lunar Radar Sounder: Intact Lunar Lava Tube Detection by LRS. *Geophysical Research Letters*, *44*(20), 10,155-10,161. https://doi.org/10.1002/2017GL074998

Kalogirou, S. A. (2009). Chapter two—Environmental Characteristics. In S. A. Kalogirou (Ed.), *Solar Energy Engineering* (pp. 49–762). Academic Press. https://doi.org/10.1016/B978-0-12-374501-9.00002-9

Kumar, P., Rawat, J. S., Rehman, S., Sajjad, H., Rani, M., Mohanto, K. K., Rai, O., & Tripathy, B. (2019). *Exploring Geomorphic Processes and Martian Gale Crater Topography on Mars using CTX and HiRISE Express Image Dataset* [Preprint]. Geosciences – Applied Geology. https://doi.org/10.5194/essd-2019-4

Lacerda, W., Ehrlich, M., Fontoura, S., & Sayão, A. (2004). *Landslides: Evaluation and Stabilization/Glissement de Terrain: Evaluation et Stabilisation, Set of 2 Volumes: Proceedings of the Ninth International Symposium on Landslides, June 28 -July 2, 2004 Rio de Janeiro, Brazil*. CRC Press. https://doi.org/10.1201/b16816

Laura, J., Acosta, A., Addair, T., Adoram-Kershner, L., Alexander, J., Alexandrov, O., Alley, S., Anderson, D., Anderson, J., Anderson, J., Annex, A., Archinal, B., Austin, C., Backer, J., Barrett, J., Bauers, J., Becker, K., Becker, T., Bennett, G., … Young, A. (2021). *Integrated Software for Imagers and Spectrometers*. Zenodo. https://doi.org/10.5281/zenodo.5347823

Le Mouélic, S., Enguehard, P., Schmitt, H. H., Caravaca, G., Seignovert, B., Mangold, N., Combe, J.-P., & Civet, F. (2020). Investigating Lunar Boulders at the Apollo 17 Landing Site Using Photogrammetry and Virtual Reality. *Remote Sensing*, *12*(11), 1900. https://doi.org/10.3390/rs12111900

Lee, C. (2019). Automated crater detection on Mars using deep learning. *Planetary and Space Science*, *170*, 16–28. https://doi.org/10.1016/j.pss.2019.03.008

697 Léveillé, R. J., & Datta, S. (2010). Lava tubes and basaltic caves as astrobiological targets on Earth and Mars: A
698 review. *Planetary and Space Science*, *58*(4), 592–598. https://doi.org/10.1016/j.pss.2009.06.004
699 Lin, C.-W., Shieh, C.-L., Yuan, B.-D., Shieh, Y.-C., Liu, S.-H., & Lee, S.-Y. (2004). Impact of Chi-Chi earthquake
700 on the occurrence of landslides and debris flows: Example from the Chenyulan River watershed, Nantou,
701 Taiwan. *Engineering Geology*, *71*(1–2), 49–61. https://doi.org/10.1016/S0013-7952(03)00125-X
702 Liu, J. G., Mason, P. J., Clerici, N., Chen, S., Davis, A., Miao, F., Deng, H., & Liang, L. (2004). Landslide hazard
703 assessment in the Three Gorges area of the Yangtze river using ASTER imagery: Zigui–Badong.
704 *Geomorphology*, *61*(1–2), 171–187. https://doi.org/10.1016/j.geomorph.2003.12.004
705 Lohse, V., Heipke, C., & Kirk, R. L. (2006). Derivation of planetary topography using multi-image shape-from-
706 shading. *Planetary and Space Science*, *54*(7), 661–674. https://doi.org/10.1016/j.pss.2006.03.002
707 Luebke, D. (2008). CUDA: Scalable parallel programming for high-performance scientific computing. *2008 5th*
708 *IEEE International Symposium on Biomedical Imaging: From Nano to Macro*, 836–838.
709 https://doi.org/10.1109/ISBI.2008.4541126
710 Luzzi, E., Rossi, A. P., Carli, C., & Altieri, F. (2020). Tectono-Magmatic, Sedimentary, and Hydrothermal History
711 of Arsinoes and Pyrrhae Chaos, Mars. *Journal of Geophysical Research: Planets*, *125*(12).
712 https://doi.org/10.1029/2019JE006341
713 Martinot, M., Besse, S., Flahaut, J., Quantin-Nataf, C., Lozac'h, L., & van Westrenen, W. (2018). Mineralogical
714 diversity and geology of Humboldt crater derived using Moon Mineralogy Mapper data. *Journal of*
715 *Geophysical Research: Planets*, *123*(2), 612–629.
716 Massa, F., & Girshick, R. (2018). *maskrcnn-benchmark: Fast, modular reference implementation of Instance*
717 *Segmentation and Object Detection algorithms in PyTorch.* https://github.com/facebookresearch/maskrcnn-
718 benchmark/
719 McEwen, A. S., Eliason, E. M., Bergstrom, J. W., Bridges, N. T., Hansen, C. J., Delamere, W. A., Grant, J. A.,
720 Gulick, V. C., Herkenhoff, K. E., Keszthelyi, L., Kirk, R. L., Mellon, M. T., Squyres, S. W., Thomas, N., &
721 Weitz, C. M. (2007). Mars Reconnaissance Orbiter's High Resolution Imaging Science Experiment
722 (HiRISE). *Journal of Geophysical Research*, *112*(E5), E05S02. https://doi.org/10.1029/2005JE002605

McEwen, A. S., Schaefer, E. I., Dundas, C. M., Sutton, S. S., Tamppari, L. K., & Chojnacki, M. (2021). Mars: Abundant Recurring Slope Lineae (RSL) Following the Planet-Encircling Dust Event (PEDE) of 2018. *Journal of Geophysical Research: Planets*, *126*(4). https://doi.org/10.1029/2020JE006575

Merghadi, A., Yunus, A. P., Dou, J., Whiteley, J., ThaiPham, B., Bui, D. T., Avtar, R., & Abderrahmane, B. (2020). Machine learning methods for landslide susceptibility studies: A comparative overview of algorithm performance. *Earth-Science Reviews*, *207*, 103225. https://doi.org/10.1016/j.earscirev.2020.103225

Merkel, D. (2014). Docker: Lightweight linux containers for consistent development and deployment. *Linux Journal*, *2014*(239), 2.

Micheletti, N., Chandler, J. H., & Lane, S. N. (2015). Structure from Motion (SfM) Photogrammetry. *Geomorphological Techniques*, 12.

Michikami, T., Hagermann, A., Miyamoto, H., Miura, S., Haruyama, J., & Lykawka, P. S. (2014). Impact cratering experiments in brittle targets with variable thickness: Implications for deep pit craters on Mars. *Planetary and Space Science*, *96*, 71–80. https://doi.org/10.1016/j.pss.2014.03.010

Milkovich, S. M., Plaut, J. J., Safaeinili, A., Picardi, G., Seu, R., & Phillips, R. J. (2009). Stratigraphy of Promethei Lingula, south polar layered deposits, Mars, in radar and imaging data sets. *Journal of Geophysical Research*, *114*(E3), E03002. https://doi.org/10.1029/2008JE003162

Miyamoto, H., Uehara, K., Murakawa, M., Sakanashi, H., Nosato, H., Kouyama, T., & Nakamura, R. (2018). Object detection in satellite imagery using 2-step convolutional neural networks. *International Geoscience and Remote Sensing Symposium (IGARSS)*, *2018-July*, 1268–1271. https://doi.org/10.1109/IGARSS.2018.8518587

Mouginis-Mark, P. J. (2004). Geometry of Martian impact craters: First results from an interactive software package. *Journal of Geophysical Research*, *109*(E8), E08006. https://doi.org/10.1029/2003JE002147

Muller, J.-P., Tao, Y., Putri, A. R. D., & Conway, S. J. (2021). 3D MULTI-RESOLUTION MAPPING OF MARS USING CASP-GO ON HRSC, CRISM, CTX AND HIRISE. *The International Archives of the Photogrammetry, Remote Sensing and Spatial Information Sciences*, *XLIII-B3-2021*, 667–671. https://doi.org/10.5194/isprs-archives-XLIII-B3-2021-667-2021

Nagle-McNaughton, T., McClanahan, T., & Scuderi, L. (2020). PlaNet: A Neural Network for Detecting Transverse Aeolian Ridges on Mars. *Remote Sensing*, *12*(21), 3607. https://doi.org/10.3390/rs12213607

751 Napieralski, J., Barr, I., Kamp, U., & Kervyn, M. (2013). 3.8 Remote Sensing and GIScience in Geomorphological
752 Mapping. In *Treatise on Geomorphology* (pp. 187–227). Elsevier. https://doi.org/10.1016/B978-0-12-
753 374739-6.00050-6
754 NASA. (2021). *NASA BRAILLE – Biologic and Resource Analog Investigations in Low Light Environments*.
755 https://nasa-braille.org/
756 Naß, A., Di, K., Elgner, S., van Gasselt, S., Hare, T., Hargitai, H., Karachevtseva, I., Kersten, E., Manaud, N.,
757 Roatsch, T., Rossi, A. P., Skinner Jr., J., & Wählisch, M. (2017). PLANETARY CARTOGRAPHY AND
758 MAPPING: WHERE WE ARE TODAY, AND WHERE WE ARE HEADING FOR? *The International*
759 *Archives of the Photogrammetry, Remote Sensing and Spatial Information Sciences*, *XLII-3/W1*, 105–112.
760 https://doi.org/10.5194/isprs-archives-XLII-3-W1-105-2017
761 Naß, A., Massironi, M., Rossi, A., Penasa, L., Pozzobon, R., Brandt, C., Nodjoumi, G., Pondrelli, M., Galluzzi, V.,
762 Altieri, F., Frigeri, A., Carli, C., Giacomoni, L., Mege, D., Gurgurewicz, J., Tesson, P.-A., Marinangeli, L.,
763 van der Bogert, C. H., & Poehler, C. (2021). *Streamlining European Mapping Efforts: The Geologic*
764 *Mapping of Planetary Bodies (GMAP)*. *2610*, 7034. https://elib.dlr.de/142475/
765 Naß, A., & van Gasselt, S. (2021). The geologic map of the Cassini quadrangle on the Moon: Planetary cartography
766 between science, efficacy and cartographic aesthetics. *International Journal of Cartography*, *7*(2), 178–
767 183.
768 Nass, A., van Gasselt, S., Hare, T., & Hargitai, H. (2021). 50 Years of Sensor-Based Planetary Cartography: Review
769 and Perspectives. *Proceedings of the ICA*, *4*, 1–8. https://doi.org/10.5194/ica-proc-4-76-2021
770 Nodjoumi, G. (2021a, October 13). *ImageProcessingUtils: Docker container, Jupyter Notebook and CLI*.
771 https://doi.org/10.5281/zenodo.5566774
772 Nodjoumi, G. (2021b). *DeepLandforms: A Deep Learning Computer Vision toolset applied to a prime use case for*
773 *mapping planetary skylights - ANc* [Data set]. https://doi.org/10.5281/zenodo.5734912
774 Nodjoumi, G. (2021c, November 29). *DeepLandforms: First Release*. https://doi.org/10.5281/zenodo.5734621
775 Nodjoumi, G., Pozzobon, R., & Rossi, A. P. (2021). DEEP LEARNING OBJECT DETECTION FOR MAPPING
776 CAVE CANDIDATES ON MARS: BUILDING UP THE MARS GLOBAL CAVE CANDIDATE
777 CATALOG (MGC^3). *Lunar and Planetary Science Conference*, *2548*.
778 https://www.hou.usra.edu/meetings/lpsc2021/pdf/1316.pdf

779 Open Geospatial Consortium. (2021). *OGC® GeoPackage Encoding Standard*. https://www.geopackage.org/spec/
780 Palafox, L. F., Hamilton, C. W., Scheidt, S. P., & Alvarez, A. M. (2017). Automated detection of geological
781 landforms on Mars using Convolutional Neural Networks. *Computers & Geosciences*, *101*, 48–56.
782 https://doi.org/10.1016/j.cageo.2016.12.015
783 Parente, M., Itoh, Y., & Saranathan, A. (2019). New CRISM Data Products for Improved Characterization and
784 Analysis of the Mars2020 Landing Site. *IGARSS 2019 - 2019 IEEE International Geoscience and Remote*
785 *Sensing Symposium*, 4911–4914. https://doi.org/10.1109/IGARSS.2019.8899313
786 Parise, M. (2019). Sinkholes. In *Encyclopedia of Caves* (pp. 934–942). Elsevier. https://doi.org/10.1016/B978-0-12-
787 814124-3.00110-2
788 Paul, S., & Ganju, S. (2021). Flood Segmentation on Sentinel-1 SAR Imagery with Semi-Supervised Learning.
789 *ArXiv:2107.08369 [Cs]*. http://arxiv.org/abs/2107.08369
790 PDS Geosciences Nodes. (2021). *Orbital Data Explorer—Mars Holdings*.
791 https://ode.rsl.wustl.edu/odeholdings/Mars_holdings.html
792 Pham, M.-T., Courtrai, L., Friguet, C., Lefèvre, S., & Baussard, A. (2020). YOLO-Fine: One-Stage Detector of
793 Small Objects Under Various Backgrounds in Remote Sensing Images. *Remote Sensing*, *12*(15), 2501.
794 https://doi.org/10.3390/rs12152501
795 Pipan, T., & Culver, D. C. (2019). Chapter 107—Shallow subterranean habitats. In W. B. White, D. C. Culver, & T.
796 Pipan (Eds.), *Encyclopedia of Caves (Third Edition)* (pp. 896–908). Academic Press.
797 https://doi.org/10.1016/B978-0-12-814124-3.00107-2
798 Pondrelli, M., Frigeri, A., Marinangeli, L., Di Pietro, I., Pantaloni, M., Pozzobon, R., Nass, A., & Rossi, A. P.
799 (2020). *Geological and geomorphological mapping of Martian sedimentary deposits: An attempt to identify*
800 *current practices in mapping and representation* [Other]. oral. https://doi.org/10.5194/epsc2020-232
801 Rashno, A., Nazari, B., Sadri, S., & Saraee, M. (2017). Effective pixel classification of Mars images based on ant
802 colony optimization feature selection and extreme learning machine. *Neurocomputing*, *226*, 66–79.
803 https://doi.org/10.1016/j.neucom.2016.11.030
804 Redmon, J., Divvala, S., Girshick, R., & Farhadi, A. (2016). You only look once: Unified, real-time object detection.
805 *Proceedings of the IEEE Computer Society Conference on Computer Vision and Pattern Recognition*.
806 https://doi.org/10.1109/CVPR.2016.91

807 Robbins, S. J., & Hynek, B. M. (2014). The secondary crater population of Mars. *Earth and Planetary Science*
808 *Letters*, *400*(2012), 66–76. https://doi.org/10.1016/j.epsl.2014.05.005
809 Robinson, M. S., Brylow, S. M., Tschimmel, M., Humm, D., Lawrence, S. J., Thomas, P. C., Denevi, B. W.,
810 Bowman-Cisneros, E., Zerr, J., Ravine, M. A., Caplinger, M. A., Ghaemi, F. T., Schaffner, J. A., Malin, M.
811 C., Mahanti, P., Bartels, A., Anderson, J., Tran, T. N., Eliason, E. M., … Hiesinger, H. (2010). Lunar
812 Reconnaissance Orbiter Camera (LROC) Instrument Overview. *Space Science Reviews*, *150*(1–4), 81–124.
813 https://doi.org/10.1007/s11214-010-9634-2
814 Robinson, M. S., Wagner, R. V., Speyerer, E. J., & Robinson, M. S. (2017). Exploring the Moon with Automated
815 Feature Detection. *Space Sci. Rev*, *129*(2), 2769.
816 Rousset, G., Despinoy, M., Schindler, K., & Mangeas, M. (2021). Assessment of Deep Learning Techniques for
817 Land Use Land Cover Classification in Southern New Caledonia. *Remote Sensing*, *13*(12), 2257.
818 https://doi.org/10.3390/rs13122257
819 Salese, F., Pondrelli, M., Neeseman, A., Schmidt, G., & Ori, G. G. (2019). Geological Evidence of Planet-Wide
820 Groundwater System on Mars. *Journal of Geophysical Research: Planets*, *124*(2), 374–395.
821 https://doi.org/10.1029/2018JE005802
822 Sargeant, H. M., Bickel, V. T., Honniball, C. I., Martinez, S. N., Rogaski, A., Bell, S. K., Czaplinski, E. C., Farrant,
823 B. E., Harrington, E. M., Tolometti, G. D., & Kring, D. A. (2020). Using Boulder Tracks as a Tool to
824 Understand the Bearing Capacity of Permanently Shadowed Regions of the Moon. *Journal of Geophysical*
825 *Research: Planets*, *125*(2). https://doi.org/10.1029/2019JE006157
826 Sauro, F., Pozzobon, R., Massironi, M., De Berardinis, P., Santagata, T., & De Waele, J. (2020). Lava tubes on
827 Earth, Moon and Mars: A review on their size and morphology revealed by comparative planetology.
828 *Earth-Science Reviews*, *209*, 103288. https://doi.org/10.1016/j.earscirev.2020.103288
829 Sauro, U. (2016). Dolines and Sinkholes: Aspects of Evolution and Problems of Classification. *Acta Carsologica*,
830 *32*(2). https://doi.org/10.3986/ac.v32i2.335
831 Servis, K., Lagain, A., Benedix, G., Flannery, D., Norman, C., Towner, M., & Paxman, J. (2020). *Automatic crater*
832 *detection over the Jezero crater area from HiRISE imagery* [Other]. pico.
833 https://doi.org/10.5194/egusphere-egu2020-6269

834 Sharma, R., & Srivastava, N. (2021). *Detection and classification of skylights on the flank of Elysium Mons, Mars*
835 [Preprint]. Geology. https://doi.org/10.1002/essoar.10506123.1
836 Silburt, A. (2019). *DeepMoon—Lunar Crater Counting Through Deep Learning* [Python].
837 https://github.com/silburt/DeepMoon (Original work published 2017)
838 Silburt, A., Ali-Dib, M., Zhu, C., Jackson, A., Valencia, D., Kissin, Y., Tamayo, D., & Menou, K. (2019). Lunar
839 Crater Identification via Deep Learning. *Icarus*, *317*, 27–38. https://doi.org/10.1016/j.icarus.2018.06.022
840 Sivakumar, V., Neelakantan, R., & Santosh, M. (2017). Lunar surface mineralogy using hyperspectral data:
841 Implications for primordial crust in the Earth–Moon system. *Geoscience Frontiers*, *8*(3), 457–465.
842 https://doi.org/10.1016/j.gsf.2016.03.005
843 Slaymaker, O., Spencer, T., & Embleton-Hamann, C. (2021). Recasting geomorphology as a landscape science.
844 *Geomorphology*, *384*, 107723. https://doi.org/10.1016/j.geomorph.2021.107723
845 Smith, Z., Tullis, J., Steele, K., & Malfavon, L. (2006). Martian Sinkholes: Implications for Large Scale Evaporite
846 Deposits. *37th Annual Lunar and Planetary Science Conference*, 1071.
847 Stepinski, T. F., Soumya Ghosh, & Vilalta, R. (2007). *Machine Learning for Automatic Mapping of Planetary*
848 *Surfaces.* https://doi.org/10.13140/2.1.1518.9445
849 Su, S., Fanara, L., Zhang, X., Gwinner, K., Hauber, E., & Oberst, J. (2021). DETECTING THE SOURCES OF ICE
850 BLOCK FALLS AT THE MARTIAN NORTH POLAR SCARPS BY ANALYSIS OF MULTI-
851 TEMPORAL HIRISE IMAGERY. *The International Archives of the Photogrammetry, Remote Sensing and*
852 *Spatial Information Sciences*, *XLIII-B3-2021*, 673–678. https://doi.org/10.5194/isprs-archives-XLIII-B3-
853 2021-673-2021
854 Sun, V. Z., & Stack, K. M. (2020). Geologic map of Jezero crater and the Nili Planum region, Mars. In *Geologic*
855 *map of Jezero crater and the Nili Planum region, Mars* (USGS Numbered Series No. 3464; Scientific
856 Investigations Map, Vol. 3464). U.S. Geological Survey. https://doi.org/10.3133/sim3464
857 Szegedy, C., Toshev, A., & Erhan, D. (2013). Deep Neural Networks for Object Detection. *Advances in Neural*
858 *Information Processing Systems 26 (NIPS 2013)*. https://doi.org/10.1109/CVPR.2014.276
859 Talukdar, S., Singha, P., Mahato, S., Pal, S., Liou, Y.-A., Rahman, A., & others. (2020). Land-use land-cover
860 classification by machine learning classifiers for satellite observations—A review. *Remote Sensing*, *12*(7),
861 1135.

862 Tempfli, K., Huurneman, G. C., Bakker, W. H., Janssen, L. L. F., Feringa, W. F., Gieske, A. S. M., Grabmaier, K.
863 A., Hecker, C. A., & Horn, J. A. van der. (2009). *Principles of remote sensing: An introductory textbook.*
864 ITC.
865 Tien Bui, D., Tuan, T. A., Klempe, H., Pradhan, B., & Revhaug, I. (2016). Spatial prediction models for shallow
866 landslide hazards: A comparative assessment of the efficacy of support vector machines, artificial neural
867 networks, kernel logistic regression, and logistic model tree. *Landslides*. https://doi.org/10.1007/s10346-
868 015-0557-6
869 Tirsch, D., Voigt, J. R. C., Viviano, C. E., Bishop, J. L., Lane, M. D., Tornabene, L. L., & Loizeau, D. (2021).
870 Spatial Trends in Mineral Abundances across Tyrrhena Terra on Mars derived from Geomorphological and
871 Mineralogical Mapping. *EGU General Assembly Conference Abstracts*, EGU21-7440.
872 Tsibulskaya, V., Hepburn, A. J., Hubbard, B., & Holt, T. (2020). Surficial geology and geomorphology of Greg
873 crater, Promethei Terra, Mars. *Journal of Maps*, *16*(2), 524–533.
874 https://doi.org/10.1080/17445647.2020.1785343
875 *Ultralytics/yolov5*. (2021). [Python]. Ultralytics. https://github.com/ultralytics/yolov5 (Original work published
876 2020)
877 Van Den Eeckhaut, M., Poesen, J., Govers, G., Verstraeten, G., & Demoulin, A. (2007). Characteristics of the size
878 distribution of recent and historical landslides in a populated hilly region. *Earth and Planetary Science*
879 *Letters*, *256*(3–4), 588–603. https://doi.org/10.1016/j.epsl.2007.01.040
880 van der Bogert, C. H., & Ashley, J. W. (2015). Skylight. In H. Hargitai & Á. Kereszturi, *Encyclopedia of Planetary*
881 *Landforms* (pp. 1–7). Springer New York. https://doi.org/10.1007/978-1-4614-9213-9_342-2
882 Wada, K. (2021). *Labelme: Image Polygonal Annotation with Python*. https://doi.org/10.5281/zenodo.5711226
883 Wang, S., Fan, Z., Li, Z., Zhang, H., & Wei, C. (2020). An Effective Lunar Crater Recognition Algorithm Based on
884 Convolutional Neural Network. *Remote Sensing*, *12*(17), 2694. https://doi.org/10.3390/rs12172694
885 Wang, Y., Wu, B., Xue, H., Li, X., & Ma, J. (2021). An Improved Global Catalog of Lunar Impact Craters (≥ 1 km)
886 with 3D Morphometric Information and Updates on Global Crater Analysis. *Journal of Geophysical*
887 *Research: Planets*, *126*(9), e2020JE006728.
888 Watkins, R., Jolliff, B., Lawrence, S., Hayne, P., & Ghent, R. (2017). *Boulder distributions at legacy landing sites:*
889 *Assessing regolith production rates and landing site hazards*.

Watters, W. A., Geiger, L. M., Fendrock, M., & Gibson, R. (2015). Morphometry of small recent impact craters on Mars: Size and terrain dependence, short-term modification. *Journal of Geophysical Research: Planets*, *120*(2), 226–254.

Whitten, J. L., & Martin, E. S. (2019). Icelandic Pit Chains as Planetary Analogs: Using Morphologic Measurements of Pit Chains to Determine Regolith Thickness. *Journal of Geophysical Research: Planets*, *124*(11), 2983–2999. https://doi.org/10.1029/2019JE006099

Wilhelm, T., Geis, M., Püttschneider, J., Sievernich, T., Weber, T., Wohlfarth, K., & Wöhler, C. (2020). DoMars16k: A Diverse Dataset for Weakly Supervised Geomorphologic Analysis on Mars. *Remote Sensing*, *12*(23), 3981. https://doi.org/10.3390/rs12233981

Wu, B., Li, F., Hu, H., Zhao, Y., Wang, Y., Xiao, P., Li, Y., Liu, W. C., Chen, L., Ge, X., & others. (2020). Topographic and Geomorphological Mapping and Analysis of the Chang'E-4 Landing Site on the Far Side of the Moon. *Photogrammetric Engineering & Remote Sensing*, *86*(4), 247–258.

Wu, Y., Kirillov, A., Massa, F., Lo, W.-Y., & Girshick, R. (2019a). *Detectron2 is FAIR's next-generation platform for object detection, segmentation and other visual recognition tasks.* https://github.com/facebookresearch/detectron2

Wu, Y., Kirillov, A., Massa, F., Lo, W.-Y., & Girshick, R. (2019b). *Detectron2/MODEL_ZOO.md at main · facebookresearch/detectron2*. https://github.com/facebookresearch/detectron2/blob/main/MODEL_ZOO.md

Wu, Y., Kirillov, A., Massa, F., Lo, W.-Y., Girshick, R., & Facebook, Inc. (2020). *facebookresearch/detectron2: Detectron2 is FAIR's next-generation platform for object detection and segmentation.* https://github.com/facebookresearch/detectron2

Wyrick, D. (2004). Distribution, morphology, and origins of Martian pit crater chains. *Journal of Geophysical Research*, *109*(E6), E06005. https://doi.org/10.1029/2004JE002240

Xiao, Z., Zeng, Z., & Komatsu, G. (2014). A global inventory of central pit craters on the Moon: Distribution, morphology, and geometry. *Icarus*, *227*, 195–201. https://doi.org/10.1016/j.icarus.2013.09.019

Yousefi, S., Pourghasemi, H. R., Emami, S. N., Pouyan, S., Eskandari, S., & Tiefenbacher, J. P. (2020). A machine learning framework for multi-hazards modeling and mapping in a mountainous area. *Scientific Reports*, *10*(1), 12144. https://doi.org/10.1038/s41598-020-69233-2

Youssef, A. M., El-Kaliouby, H., & Zabramawi, Y. A. (2012). Sinkhole detection using electrical resistivity tomography in Saudi Arabia. *Journal of Geophysics and Engineering*, *9*(6), 655–663. https://doi.org/10.1088/1742-2132/9/6/655

Zhang, A., Lipton, Z. C., Li, M., & Smola, A. J. (2021). 4.4.3 Underfitting or Overfitting? In *Dive into Deep Learning* (pp. 146–147). http://arxiv.org/abs/2106.11342

Zhao, Z. Q., Zheng, P., Xu, S. T., & Wu, X. (2019). Object Detection with Deep Learning: A Review. In *IEEE Transactions on Neural Networks and Learning Systems* (Vol. 30, Issue 11, pp. 3212–3232). https://doi.org/10.1109/TNNLS.2018.2876865